Kobe University Repository : Kernel

PDF issue: 2025-12-04

Effects of oblique impacts on the impact strength of porous gypsum and glass spheres: Implications for the collisional disruption of planetesimals in thermal evolution

Yasui, Minami
Arakawa, Masahiko
Yoshida, Yusaku
Matsue, Kazuma
Takano, Shota

(Citation)
Icarus,335:113414

(Issue Date)
2020-01-01

(Resource Type)
journal article

(Version)
Accepted Manuscript

(Rights)
© 2019 Elsevier Inc.
This manuscript version is made available under the CC-BY-NC-ND 4.0 license
http://creativecommons.org/licenses/by-nc-nd/4.0/

(URL)
https://hdl.handle.net/20.500.14094/90006963

Effects of Oblique Impacts on the Impact Strength of Porous Gypsum and Glass Spheres: Implications for the Collisional Disruption of Planetesimals in Thermal Evolution

Minami Yasui, Masahiko Arakawa, Yusaku Yoshida, Kazuma Matsue, Shota Takano

Graduate School of Science, Kobe University

1-1, Rokkodai-cho, Nada-ku, Kobe, Hyogo 657-8501, Japan

Tel: +81-78-803-5741

Fax: +81-78-803-5741

E-mail: minami.yasui@pearl.kobe-u.ac.jp

Manuscript pages: 63

Number of figures: 16

Number of tables: 4

Proposed running head: Oblique impacts of planetesimals in thermal evolution

Corresponding author:

Minami Yasui

Now at

Graduate School of Science, Kobe University

1-1, Rokkodai-cho, Nada-ku, Kobe, Hyogo 657-8501, Japan

Tel: +81-78-803-5741

Fax: +81-78-803-5741

E-mail: minami.yasui@pearl.kobe-u.ac.jp

Abstract

We conducted oblique impact experiments for porous gypsum spheres and glass spheres simulating primitive and consolidated rocky planetesimals, respectively, and we determined the effects of the impact angle on the impact strength of these rocky planetesimals. The targets were a porous gypsum sphere with a porosity of 50% and a glass sphere without porosity. A spherical polycarbonate projectile impacted the target at 2–7 km s^{-1} at an impact angle, θ, ranging from 90° (head-on collision) to 10° (grazing collision) by using a two-stage light-gas gun at Kobe University, Japan. The impact strength obtained at a head-on collision was 1330 J kg^{-1} for the porous gypsum target and 1090 J kg^{-1} for the glass target, and these values increased markedly with the decrease of the impact angle when the impact angle was smaller than a critical angle, θ_c; the obtained θ_c values were 30° for the porous gypsum target and 55° for the glass target. The normalized largest fragment mass (m_l/M_t) showed a good correlation with an effective specific energy ($Q_{eff} = Q \sin^2 \theta$); the subsequent empirical equation was $m_l/M_t = 10^{2.02} {Q_{eff}}^{0.76}$ for the porous gypsum target and $m_l/M_t = 10^{4.66} {Q_{eff}}^{1.68}$ at m_l/M_t <0.75 and $m_l/M_t = 10^{0.12} {Q_{eff}}^{0.08}$ at m_l/M_t >0.75 for the glass target. Based on our

experimental results, we successfully introduce the effects of an oblique impact on the degree of disruption for primitive and consolidated rocky planetesimals. Our findings demonstrate that in a strength-dominated regime, the catastrophic disruption can occur over a wide range of impact angles (30°–90°) irrespective of the target materials, when the specific energy at the collision is about four times larger than the impact strength.

Keywords: Collisional physics; Impact processes; Planetesimals; Planetary formation

1. Introduction

Solar system bodies are believed to grow via collisional disruption and re-accumulation processes among planetesimals that are in their early evolution. Planetesimals are speculated to have various porosities depending on their thermal evolution stages [e.g., *Neumann et al*., 2012; *Henke et al*., 2012; *Lichtenberg et al.*, 2016]. For example, planetesimals are believed to be parent bodies of porous asteroids and cometary nuclei, and they could therefore also be highly porous bodies [e.g., *Weidenschilling*, 1994, 2011; *Asphaug et al.*, 2002; *Sierks et al.*, 2011]. However, some planetesimals could experience various thermal processes such as shock metamorphism and aqueous alteration during their evolution so that they evolved to be low-porous or non-porous bodies. For the study of the collisional accretion processes of planetesimals in the solar nebula, the catastrophic disruption and the re-accumulation processes should be clarified for planetesimals that have various porosities depending on their thermal evolution.

There have been many experimental studies on the collisional processes of planetary bodies in attempts to determine the impact strength and the impact conditions for

catastrophic disruption and to measure the ejection velocity distribution of the impact fragments, which is necessary for estimating the re-accumulation conditions. The prior studies manipulated both projectile and target materials, and used basalt, glass, porous gypsum, ice, and snow to examine the effects of porosity, inclusion, and static strength on the impact strength. The size ratio of the projectile to the target, the target shape, the target rotation rate, and the impact velocity were also manipulated to elucidate how these parameters affect the impact strength and the ejection velocity of impact fragments [e.g., *Gault and Wedekind*, 1969; *Fujiwara et al.*, 1977; *Kawakami et al.*, 1983; *Arakawa*, 1999a; *Arakawa et al.*, 2002; *Okamoto and Arakawa*, 2009; *Yasui and Arakawa*, 2011; *Morris and Burchell*, 2017]. Impact strength is defined as a specific energy when the largest fragment mass is one-half of the original target mass, and the specific energy is defined as the kinetic energy of the impactor per unit mass of the target.

It has been suspected that during the collisional evolution of planetesimals, they collided obliquely with each other; this expectation arose because *Shoemaker* [1962] calculated the probability of oblique impacts, P, among planetary bodies in the solar system as $dP = 2\sin\theta\cos\theta d\theta$, where θ is the impact angle. Shoemaker demonstrated

that when the normal impact was defined as 90°, impact angle showing the maximum frequency was 45° and the probability of collisions at an impact angle <70° was approximately 90%. Many numerical simulations have thus been conducted for planetesimal collisions at various impact angles [e.g., *Leinhardt and Richardson*, 2002; *Movshovitz et al.*, 2016; *Genda et al.*, 2017], but only a few experimental studies have been conducted to investigate the effect of the impact angle [e.g., *Fujiwara and Tsukamoto*, 1980; *Nakamura,* 1993; *Arakawa,* 1999a]. Most of the experimental studies examined head-on collisions; only a few experimental studies have investigated the effect of the impact angle. It is necessary to study oblique impacts in the laboratory in order to confirm and improve these numerical studies.

A few experimental studies have investigated the effect of the impact angle on the impact strength and the ejection velocity of impact fragments. *Fujiwara and Tsukamoto* [1980] conducted impact experiments using spherical basalt targets at the impact velocity of 2.5–2.9 km s^{-1} and at impact angles from 0° to 60° (their impact angle of 0° indicates a head-on collision). They obtained the relationship between the mass fraction of the largest fragment to the original target and the specific energy, and they observed that the

mass fraction increased with the increase of the impact angle at a constant specific energy. They also obtained the relationship between the fragment velocity at the antipodal point of the impact point on the target and the specific energy, and they observed that the antipodal velocity for an oblique impact was lower than that for a head-on collision. *Nakamura* [1993] also conducted impact experiments using spherical basalt targets at the impact velocity of 3.1–3.6 km s^{-1} and at impact angles from 30° to 90° (her impact angle of 90° indicates a head-on collision). She obtained three-dimensional fragment velocities and the cumulative mass distribution of impact fragments. However, both *Fujiwara and Tsukamoto* [1980] and *Nakamura* [1993] carried out only five or six shots for oblique impacts, because they conducted mainly head-on impact experiments. It is thus difficult to discuss the effects of the impact angle on the impact strength and the ejection velocity of impact fragments quantitatively.

Arakawa [1999a] conducted impact experiments in a cold room at –18°C by using spherical H_2O ice targets at the impact velocity of 0.17–0.64 km s^{-1} and at impact angles from 0° to 50° (his impact angle of 0° indicates a head-on collision). He studied the ejection velocity distribution of impact fragments ejected from different positions on the

target surface, and he observed that the position showing the minimum ejection velocity gradually shifted from the antipodal point to the upstream direction as the impact angle was increased. He also noted that the minimum ejection velocity decreased with the increase of the impact angle. He obtained an empirical equation for the minimum ejection velocity, $V_{\min}$, related to the impact angle, ϕ, as $V_{\min} = 49(\cos\phi)^{3.4}$, but he did not study the effect of oblique impacts on the impact strength of the ice target. Systematic impact experiments investigating catastrophic disruption by oblique impacts are thus necessary to determine not only the impact strength but also the ejection velocity of impact fragments.

In this study, we conducted oblique impact experiments to study the effects of the impact angle on the impact strength and the ejection velocity of impact fragments. We systematically changed the impact angle from a head-on collision to a grazing collision. We greatly increased the number of experiments for oblique impacts compared to three previous works [*Fujiwara and Tsukamoto*, 1980; *Nakamura*, 1993; *Arakawa*, 1999a] in order to determine the catastrophic disruption of oblique impacts quantitatively. We used a porous gypsum target and a glass target for the experiments to simulate the collision of

rocky planetesimals in thermal evolution: the porous gypsum target simulated primitive rocky planetesimals with high porosity before thermal evolution, and the glass target simulated consolidated rocky planetesimals after thermal evolution. Based on our experimental results and the theory of oblique impacts on planetary bodies described by *Shoemaker* [1962], we also discuss the relationship between the impact probability and the degree of impact disruption for rocky planetesimals depending on the thermal evolution in the solar system.

2. Experimental Methods

2.1. The targets and projectile

We used a porous gypsum sphere and a glass sphere as targets simulating primitive and consolidated rocky planetesimals, respectively. These materials have been used in other laboratory experiments as the analogs of primitive and consolidated planetesimals that have experienced thermal evolution at various stages [e.g., *Gault and Wedekind*, 1969; *Love et al.*, 1993; *Onose and Fujiwara*, 2004; *Fujii and Nakamura*, 2009; *Kadono et al.*, 2009; *Nakamura et al.*, 2009; *Okamoto and Arakawa*, 2009; *Heißelmann et al.*,

2010; *Yasui and Arakawa*, 2011; *Yasui et al.*, 2012].

The porous gypsum sphere was prepared as follows. Commercial $CaSO_4 \cdot 1/2H_2O$ powder (Nitto Co., Ltd.) was mixed with tap water, and the mixed slurry was then put into a spherical mold. The target was hung by a string in a recovery box, and a small clip for hanging the string was set on the surface of the mixed slurry in the mold. After the slurry was consolidated, the porous gypsum sphere was pulled out from the mold. It was dried in an oven at 55°C for 2–7 days to complete the chemical reaction to $CaSO_4 \cdot 2H_2O$ and to remove excess water inside the sphere. The porosity of the porous gypsum spheres was thus regulated at 55±6%; the bulk density was 983±131 kg m^{-3}. The tensile strength and the bulk sound velocity of the porous gypsum changed from 2.56 MPa and 1.46×10^3 m s^{-1} at the porosity of 49% to 1.01 MPa and 1.19×10^3 m s^{-1} at the porosity of 61%. Although the impact strength and the ejection velocity of impact fragments could be controlled by the porosity, i.e., the tensile strength, we found that a porosity variation of 10% or less did not affect the impact strength and the ejection velocity very much. The diameter of the porous gypsum spheres was changed from 40 to 70 mm in 10 mm steps, and the spheres with diameters of 40 and 60 mm were used only for the head-on collision

because the specific energy was changed in the wide range to determine the impact strength accurately.

The glass spheres were commercially available synthetic quartz glass spheres with diameters of 30, 50, 60, and 80 mm (Nichika Inc.), and the 60 mm-diameter sphere was used only for the head-on collision. The bulk density of the glass spheres was measured as 2513±33 kg m^{-3}. The bulk sound velocity of each glass sphere was 4.20×10^3 m s^{-1}. The reported tensile strength of soda lime glass, 31–35 MPa, was taken as the tensile strength for the glass sphere, since the bulk densities of the glass spheres were very similar to those of soda lime glass [*Ashby*, 2013]. A lattice pattern was painted on the target surface with black ink to identify the original position of each impact fragment recovered after the shot. The projectile was a polycarbonate sphere with a diameter of 4.73 (±0.01) mm and a mass, m_{p}, of 67.9 (±0.1) mg.

2.2. Impact experiments

We conducted impact experiments by using a two-stage light-gas gun set at Kobe University. Fig. 1 is a schematic illustration of the experimental setup. The vacuum

Fig. 1

chamber was evacuated at approximately 20 Pa before the shot. The impact angle, θ, was changed from 9° to 90°. The θ is defined as the angle between the line perpendicular to the projectile trajectory and the line linking the center of the target and the impact point on the target surface, as shown in Fig. 2a. We measured the impact angle by using images taken by a shutter camera or a high-speed camera. The offset of the projectile trajectory in the sight of the view is within the projectile's radius so we could ignore the offset to determine the impact angle. An overview of the method used to measure the impact angle θ is shown in Figs. 2b and 2c. When the shutter camera was used with an exposure time of 100 ns (Fig. 2b), two images were taken at different times before the impact, and the impact point on the target surface was determined as an intersection point of the projectile trajectory on the target surface.

Fig. 2

When the high-speed camera was used (Fig. 2c), the frame rate (10^4 frames s^{-1}) was too low to determine the projectile trajectory. We thus estimated the impact point on the target surface by using the envelope of fine fragments ejected from the impact point just after the impact. In this case, we assumed that the fine fragments were ejected in axial symmetry against the line connecting the impact point to the target center, and we were

able to determine the ejecta neck from the fine fragments as shown in the left image of Fig. 2c. The impact point was then set at the middle point on the line linking both ejecta necks.

We defined a head-on collision as an impact with $\theta = 80°–90°$. The impact velocity, v_{i}, for oblique impacts was 3.8 and 6.9 km s^{-1} for the porous gypsum targets, and 4.3, 4.9, and 5.9 km s^{-1} for the glass targets. For the head-on collisions, we systematically changed the impact velocity from 2.2 to 6.9 km s^{-1} for both types of targets. The measured error of impact velocity was ≤1%. The specific energy, Q, is usually used as a parameter representing the impact condition, and it is defined by using the projectile mass, m_{p}, the original target mass, M_{t}, and the impact velocity v_{i} as $Q \equiv \frac{1}{2} m_{\mathrm{p}} {v_{\mathrm{i}}}^2 / \left(M_{\mathrm{t}} + m_{\mathrm{p}}\right)$. For the porous gypsum targets, the specific energy Q was approximately 3×10^3 and 10^4 J kg^{-1} for the oblique impacts. For the glass targets, the Q was approximately 10^3, 2×10^3, and 4×10^3 J kg^{-1} for the oblique impacts.

The target was set in an acrylic recovery box to collect the impact fragments after the shot. Four of the six inside walls of the recovery box were covered with sponge plates to prevent impact fragments from secondary collisions on the inside walls. The other two

inside walls were not covered, in order to allow observation by the high-speed camera and shutter camera. The target was set in the recovery box by using strings passing through a hole in the clip on the target. Most of the porous gypsum targets were suspended from the top of the box (Fig. 2c). The glass targets and several porous gypsum targets were set on a string net resembling a hammock (Fig. 2b). After each shot, we recovered the impact fragments and measured their masses with an electrical mass balance. We measured the fragments one by one to identify fragments with masses ≥0.01 g, and we sieved the fragments with masses <0.01 g into four groups according to the mesh sizes of the sieves: 2.0 mm, 1.4 mm, and 1.0 mm, and <1.0 mm. We measured the total mass of each size group.

The collisional disruption of the target was observed by a high-speed camera (RX-6; NAC Image Technology, Tokyo) set at the side of a vacuum chamber. The frame rate and the shutter speed were set at 10^4 frames s^{-1} and 10 or 20 μs, respectively. We used a metal halide lamp to illuminate the target from the side at which the camera was placed or from the side behind the recovery box (Fig. 1). We used the images taken by the high-speed camera for the analysis of the fragment velocity distribution, although some fragments

hit the strings and the velocity distribution was disturbed. We thus used only the images taken during the period before fragments hit the strings for the analysis of the fragment velocity distribution.

3. Experimental Results

3.1. Observations of collisional disruption

Table 1

Table 2

Fig. 3

The experimental conditions and the results of each shot are summarized in Table 1 for the porous gypsum targets and in Table 2 for the glass targets. Fig. 3 provides snapshots of the collisional disruption of a porous gypsum target taken by the high-speed camera impacted at the specific energies of 3×10^3 J kg^{-1} (Fig. 3a–c) and 10^4 J kg^{-1} (Fig. 3d–f). The impact angle θ is 75° in Fig. 3a and 3d, 45°–55° in Fig. 3b and 3e, and 10°–15° in Fig. 3c and 3f. As shown in the second image in each panel, cloudy ejecta composed of fine dust formed and grew as a U-shaped ejecta curtain from the impact point just after the projectile impacted. At a large impact angle (75° or 45°–55°), many cracks were radially generated around the impact point, and pyramid-shaped fragments were ejected after 0.5–5 ms of the impact, as shown in the third to the fourth images of

Fig. 3 (panels a, b, d, and e).

At the low specific energy of 3×10^3 J kg^{-1}, large fragments formed around the antipodal point and moved slowly toward the downstream region of the projectile trajectory, and the other fragments scattered outward from the original position within 20 ms of the impact as shown in the fourth image of Fig. 3a and 3b. At the high specific energy of 10^4 J kg^{-1}, the target was disrupted catastrophically and the fragments expanded in the downstream direction (fourth images in Fig. 3d and 3e), then scattered in all directions as shown in the fifth images. In contrast, with a small impact angle (10°–15°), several large fragments were ejected from the impact point as shown in the third image in Fig. 3c and the fourth image in Fig. 3f. Within 10 to 20 ms of the impact, the largest fragment moved upward and slowly rotated counterclockwise. No cracks were observed on the surface of target for the low specific energy (Fig. 3c).

Fig. 4 presents snapshots of the glass targets at the specific energies of 10^3 J kg^{-1} and at 4×10^3 J kg^{-1}. The impact angle θ is 80° in Fig. 4a and 4d, 40°–45° in Fig. 4b and 4e, and 15° in Fig. 4c and 4f. Just after the impact (as shown in the second images), dusty fine fragments were ejected from the impact point to form an envelope resembling a pillar

Fig. 4

growing in the upstream direction along the line connecting the impact point with the target center, and the pillar-type ejecta were quite different from the U-shaped ejecta curtain formed on the porous gypsum targets. Surprisingly, fine fragments were also ejected from the antipodal point, and we observed a symmetrical, cone-shaped ejecta envelope around the antipodal point (Fig. 4, third images). This antipodal ejecta curtain became more pronounced as the impact angle grew closer to a head-on collision. The entire target was completely fractured and filled with cracks, becoming opaque (except for the target at the low specific energy and $\theta = 15°$ as shown in Fig. 4c, as this glass target was transparent before the shot). With the low specific energy and $\theta = 15°$, the cone-type curtain did not appear at the antipodal point, but several fragments ejected. At 3 ms after the impact (Fig. 4, fourth images), many small but resolved fragments appeared in the image and were ejected from both the impact point and the antipodal point in the upstream and the downstream directions, respectively. At 20 ms after the impact (Fig. 4, fifth images), the fine fragments scattered away, but the largest fragment remained at the center of the image.

3.2. Ejecta velocity distributions of impact fragments

As noted above in Section 3.1, the impact fragments were ejected in different forms depending on the target materials. We therefore analyzed the ejecta velocity distribution depending on the initial surface position to characterize the kinetics of the impact fragments for both types of target. We did not measure individual fragment velocities directly; instead we made two types of velocity measurement. One measurement was of the expanding velocity of the ejecta envelope consisting of the fine fragments at high specific energy. The other measurement was of the ejection velocity of the impact fragments from the antipodal point (hereinafter the antipodal velocity).

The obtained high-speed images were too blurred to distinguish each fragment in the cases of the catastrophic disruption of the target, due to the hazy created by tiny fragments; it was thus difficult to trace each fragment. We therefore usually measured the expanding velocity of the ejecta envelope as a representation of the velocity of fragments ejected from the target surface at different positions. This expanding velocity was obtained by an analysis of the successive images gathered at a few milliseconds after the impact. We assumed that these tiny fragments comprising the envelope were ejected

Fig. 5

radially from the impact point as in the "radial point model" proposed by *Paolicchi et al.* [1989] and that the fragments did not have the velocity component of the line-of-sight direction shown in Fig. 3d–f and Fig. 4d–f. We then defined the line connecting the target center with the projectile center at the impact as the base line in order to determine the initial position angle, and thereby the initial surface position, for each fragment. The base line was set at 0° as shown in Fig. 5a.

As we assumed that the surface fragments were ejected radially from the impact point, we set the impact point as the origin, and drew measurement lines from the origin at successive increments of 15° (15°, 30°, etc.) from the base line (Fig. 5a). We defined the region where the projectile was directed as the downstream region and set a minus (–) angle. We defined the opposite region as the upstream region and set a plus (+) angle. This analysis method is the same as that used by *Arakawa* [1999a].

Fig. 5 (panels b and c) illustrates the relationship between the expanding velocity and the initial position angle for the porous gypsum and glass targets. The velocity distributions of the ejecta envelope were quite different between the porous gypsum and glass targets. With the porous gypsum targets, the expanding velocity grew larger as the

initial position angle increased in the case of a head-on collision, and the expanding velocity distributions were almost axisymmetric to the initial position angle of 0°: the expanding velocity became the minimum at the initial position angle of 0°. At the impact angles of 20° and 55°, the expanding velocity distribution was no longer axisymmetric, so that the minimum expanding velocity appeared at the initial position angle at +30°. The minimum expanding velocity for each impact angle decreased from 10 m s^{-1} for the head-on collision to 2 m s^{-1} for the highly oblique impact of 20°. In addition, the velocities expanding in the downstream direction were higher than those expanding in the upstream direction at oblique impacts.

These observed characteristics of expanding velocity distributions are very similar to those of ice-ice oblique impacts observed by *Arakawa* [1999a]. In the present study, the results of the highly oblique impact of 15° showed that the expanding velocity did not depend on the initial position because the degree of disruption was not very severe, and then several large fragments remained; a few fragments were measured in this case.

The expanding velocity distribution of the glass targets was axisymmetric to the initial position angle of 0° not only for the head-on collision but also for the highly oblique

impacts. The expanding velocity was the maximum at the initial position angle of 0°, and it decreased toward the initial position angle close to ±60°. The velocity then slightly increased from 60° to 75°, irrespective of the impact angle (Fig. 5d). This slight increase of the expanding velocity around 60°–75° can be simply explained by the ejecta curtain formed around the impact point (as shown in the third images of Fig. 4). The expanding velocity at the initial position angle of 0° increased with the increase of the impact angle, but the expanding velocity at an initial position angle beyond ±30° was almost the same, irrespective of the impact angle. These observed characteristics of the glass targets were quite different from those of the porous gypsum targets, with the most notable difference being that the expanding velocity of the glass targets was the maximum at the antipodal point and rapidly decreased toward ±30°.

When *Gault and Wedekind* [1969] conducted impact experiments using crystal glass balls at impact velocities up to 7.6 km s^{-1}, they reported that the impact fragment was ejected from the antipodal point with the highest velocity among all fragments. Their results were very similar to our present results using a glass target. This high expanding velocity at the antipodal point could be caused by a shock wave concentration near the

antipodal point on the glass target surface, because the glass target in our study had a perfect spherical shape with a very smooth surface and a homogeneous interior.

Several previous works measured the antipodal velocity as a representative velocity of the low-velocity fragments for various target materials [*Fujiwara and Tsukamoto*, 1980; *Arakawa*, 1999a; *Okamoto and Arakawa*, 2009; *Yasui and Arakaw*a, 2011]. We therefore measured the antipodal velocity, V_a, of porous gypsum and glass targets to investigate the effects of the impact angle on the antipodal velocity. We compare the V_a values of our porous gypsum targets with the values in previous studies in Fig. 6. It should be noted that the minimum ejection velocity was sometimes inconsistent with the antipodal velocity in the oblique impact, as discussed above.

Fig. 6

Fig. 6 illustrates the relationship between the antipodal velocity V_a in the laboratory coordinate system and the specific energy Q for the porous gypsum targets. The V_a for the porous gypsum targets was constant for a given Q value at the impact angle θ ≥40°, while at the θ ≤30°, the V_a greatly decreased with the decrease of the θ: the V_a at the θ of 10° or 15° was an order of magnitude smaller than that at the θ of 90°. The V_a at the impact angles ≥40° increased with the increase of the Q, and the V_a could be fitted

by a power law equation as follows:

$$V_{\mathrm{a}} = 10^{-2.21\pm0.17} Q^{0.80\pm0.04}. \qquad (1)$$

Our experimental results at the impact angles ≥40° were consistent with the previous results for head-on collisions of porous gypsum targets with the porosity of 53±4%, but the previously reported values for non-porous materials such as H_2O ice and basalt were several times larger than our present findings, although the power law indices of the Q for the empirical equations in Fig. 6 were approximately 0.8, irrespective of the materials. The effect of the impact angle on the antipodal velocity is somewhat limited for porous gypsum targets; that is, the V_{a} only for highly oblique impacts with the θ <40° was several times smaller than that for the head-on collision, and the V_{a} strongly depended on the impact angle at the θ <40°.

One of the most impressive ejecta features observed on the glass targets was the abnormal high velocity fragments that jetted from the antipodal point. Fig. 7 shows the relationship between the antipodal jet velocity, V_{jet}, and the specific energy Q for the glass targets, where the V_{jet} is the expanding velocity at the antipodal point as shown in Fig. 4. The V_{jet} had an almost constant value of 182±47 m s^{-1} except for the impact angle

Fig. 7

of 15°, irrespective of the Q, and this velocity is much higher than the velocity of the center-of-mass for each impact. The jetting mechanism at the antipodal point could be very complicated related to the shock wave spreading through the target interior and focusing at the antipodal point. Detailed numerical simulations may help reconstruct this feature. Such detailed study is beyond the scope of the present investigation. However, a simple estimate of the pressure focusing at the antipodal point, P_{a}, can be made by using the V_{jet} and the Hugoniot of glass according to the equation $P_{\mathrm{a}} \approx \rho C_{\mathrm{b}} V_{\mathrm{jet}}/2$, where ρ and C_{b} are the density of glass, 2,500 kg m^{-3}, and the bulk sound velocity of glass, 4×10^3 m s^{-1} [*Melosh*, 1989]. The antipodal pressure inducing the jetting is estimated as approximately 1 GPa, which is rather higher than the tensile strength of glass, 31–35 MPa [*Ashby*, 2013].

3.3. Mass frequency distribution of the recovered fragments

Fig. 8 provides photographs of the recovered fragments of the porous gypsum targets. The impact angle θ was 75° in Fig. 8a and 8d, 40°–45° in Fig. 8b and 8e, and 10°–15° in Fig. 8c and 8f. The applied specific energy is ~3×10^3 J kg^{-1} for Fig. 8a–c and ~10^4 J

Fig. 8

kg^{-1} for Fig. 8d–f. A comparison of the photos of the recovered fragments at the different specific energies but a similar impact angle reveals that the degree of the impact disruption is not very different, although the degree of the impact disruption changes greatly with the impact angle. The targets were disrupted catastrophically at $\theta = 75°$ and 40°–45°, and it can be seen in Fig. 8 that the large fragments have a conical shape and/or a curved surface with a black marker line, which means that they originated near the target surface including the antipodal point.

Although core-type fragmentation is usually observed for non-porous rocky materials such as basalt [*Fujiwara et al.*, 1977], we did not observe this type of fragmentation for the porous gypsum targets—even with the oblique impacts— possibly because the rear-surface spallation was reduced due to the strong decay of shock pressure in porous targets [*Love et al.*, 1993; *Okamoto and Arakawa*, 2009]. The smaller fragments could have originated mainly around the impact point, as recognized in the high-speed image in Fig. 3. In the case of the highly oblique impact at the θ of 10°–15°, a large crater with a diameter of approximately 20 mm was observed on the target surfaces, and the crater was recognized to be composed of a small pit surrounded by a spalling area.

Fig. 9 shows the photographs of the recovered fragments for glass targets. The impact angle θ was 80° in Fig. 9a and 9d, 40° in Fig. 9b and 9e, and 15° in Fig. 9c and 9f. The applied specific energy was ~10^3 J kg^{-1} for Fig. 9a–c and ~4×10^3 J kg^{-1} for Fig. 9d–f. The recovered fragments of the glass targets were clearly different from those of the porous gypsum targets; i.e., the degree of the impact disruption for the glass targets changed with not only the specific energy but also the impact angle. At the low specific energy, the glass targets were partially disrupted around the impact point, and the antipodal point became truncated at both sides as shown in the expanded windows of Fig. 9a–c. In addition, many cracks were generated inside the targets so that the impacted area looked white due to the large number of small cracks.

Fig. 9

At the large specific energy, the glass targets were disrupted catastrophically, and the size of the largest fragment became smaller as the impact angle grew larger. It was also apparent that the amount of small fragments decreased with the decrease of the impact angle. The high-speed images in Fig. 4 showed that large fragments originated from the middle part of the target, and small fragments originated around the impact point and the antipodal point. However, we did not observe core-type fragmentation for our glass

targets at any of the impact angles and specific energies, as was reported for basalt [*Fujiwara et al.*, 1977]. The fragmentation mode of our glass targets changed directly from the truncated fragmentation at low specific energy to catastrophic disruption at high specific energy.

Fig. 10 shows the mass frequency distributions of the impact fragments at different impact angles; they are described by the relationship between the cumulative number of impact fragments, N, and the fragment mass normalized by the original target mass, m/M_{t}, for porous gypsum targets at the specific energy of 3×10^3 J kg^{-1} and for glass targets at the specific energy of 4×10^3 J kg^{-1}. The m/M_{t} at N=1 on the mass frequency distribution indicates the largest fragment mass normalized by the original target mass, $m_{\mathrm{l}}/M_{\mathrm{t}}$. In the case of the porous gypsum targets shown in Fig. 10a, the mass frequency distributions obtained at the impact angle ≥45° were almost the same, and thus the mass frequency distribution can be described by the same power law equation. When the impact angle was changed from 45° to 10°, the amount of impact fragments was reduced with the decrease of the impact angle. However, the slopes of the mass frequency distribution at the m/M_{t} values smaller than 10^{-3} did not systematically depend on the

Fig. 10

impact angle.

For the glass targets shown in Fig. 10b, the mass frequency distributions obtained for the impact angles ≥40° were almost the same. When the impact angle was changed from 40° to 15°, the amount of impact fragments was slightly reduced within a factor of two. Notably, the slope of the mass frequency distribution at the m/M_{t} values smaller than 10^{-3} was almost the same, and this is described by the power law equation, $N \propto (m/M_{\mathrm{t}})^{-\alpha}$ [*Takagi et al.*, 1984]. The mass frequency distributions of our porous gypsum and glass targets at the m/M_{t} values $<10^{-3}$ were fitted by the power law equation, and we observed that the α values did not strongly depend on the impact angle and the specific energy, as shown in Fig. 10c. Thus, the average α was 0.75±0.07 for the porous gypsum targets and 0.95±0.08 for the glass targets: the α for the porous gypsum targets might be smaller than that for the glass targets. These values are larger than that for polycrystalline ices at 0.64±0.06 obtained by *Arakawa* [1999b], and that for basalt at 0.54±0.16 obtained by *Takagi et al.* [1984].

3.4. Largest fragment mass and impact strength

The largest fragment mass among all impact fragments is a good representative of the degree of impact fragmentation. We thus examined the relationship between the largest fragment mass normalized by the original target mass, m_l/M_t, and the impact angle θ for the porous gypsum and glass targets as shown in Fig. 11, where we use the term NLFM for the normalized largest fragment mass, m_l/M_t. For both types of target, the NLFM was nearly constant or slightly increased with the decrease of the impact angle at the high-impact angle region in all specific energies, and the NLFM values were almost the same as the NLFM obtained for the head-on collision within a factor of two.

Fig. 11

In contrast, the NLFM increased with the decrease of the impact angle at the low-impact angle region, and the NLFM rose more rapidly as the specific energy was larger. It is quite clear that this quasi-constant NLFM region extended from the head-on collision (θ = 90°) toward the low-impact angle region, and thus this quasi-constant region continued until 30° for the porous gypsum targets and 55° for the glass targets. We defined those impact angles at the boundary of the quasi-constant NLFM region as the critical angle, θ_c, and this angle does not depend on the specific energy.

Generally, the NLFM has a good relationship with the specific energy for head-on

collisions; it is fitted by the following power law equation:

$$\frac{m_{\mathrm{l}}}{M_{\mathrm{t}}} = 10^{p_1} \cdot Q^{-q_1}. \qquad (2)$$

The impact strength, Q^*, is defined as the specific energy when the NLFM is equal to 0.5. Fig. 12 illustrates the relationship between the NLFM and the specific energy for the porous gypsum targets and glass targets. For the porous gypsum targets, the NLFM at the impact angle from 90° to 45° was almost the same, although it fluctuated slightly within a factor of two. The NLFM at the very low impact angle clearly deviated from these high impact angle data. Similarly, for the glass targets, the NLFM at the impact angle from 90° to 60° was almost the same, but the NLFM at the impact angles lower than 45° was clearly larger than these high impact angle data at the same Q. We observed that the glass targets began to be fractured and the truncated regions appeared on both the impact and the antipodal points at the specific energy of approximately 10^3 J kg^{-1}.

Fig. 12

We then derived the impact strength Q^* for a head-on collision (θ of 90° and 80°), and the results in Fig. 12 were thus fitted by using Eq. (2) at the NLFM values <0.75. The parameters p_1 and q_1 and the obtained Q^* for the porous gypsum and glass targets are summarized in Table 3. We observed that the Q^* of the porous gypsum targets was

Table 3

slightly larger than that of the glass targets, although the static tensile strength of the porous gypsum (~1 MPa from *Yasui and Arakawa* [2011]) was one order of magnitude smaller than that of the glass (31–35 MPa from *Ashby* [2013]). This inconsistency between the static and dynamic strength may have been caused by the low shock-induced pressure and the large attenuation rate of shock pressure for porous materials [*Kawakami et al.*, 1991]. Moreover, it is impressive that the power of Eq. (2), q_1, for glass targets was approximately 2.5 times larger than that for porous gypsum targets. This means that a small change of specific energy can cause a drastic change in the degree of the impact fragmentation for glass targets.

For a comparison of our results for porous gypsum and glass targets with the findings of earlier studies, the previous results for porous gypsum with a porosity of 53±4% obtained by *Okamoto and Arakawa* [2009] and for basalt obtained by *Fujiwara and Tsukamoto* [1980] are also shown in Fig. 12 and Table 3. As explained in Fig. 12, our NLFM values for the porous gypsum targets were somewhat smaller than those obtained by *Okamoto and Arakawa* [2009] over the range of the specific energy in the present study, but the power of Eq. (2), q_1, for our porous gypsum targets was almost the same

as that obtained by *Okamoto and Arakawa* [2009]. When our glass targets are compared with the basalt studied by *Fujiwara and Tsukamoto* [1980], it is apparent that the power of Eq. (2), q_1, for our glass targets is not very different from that of basalt, and the NLFM values of these two types of material were very similar, and thus the materials' impact strengths were almost the same.

4. Discussions

4.1. Effective specific energy

As described above in Section 3.4., we observed that the impact strength for a head-on collision was approximately 1000 J kg^{-1} for both types of target, while the NLFM increased with the decrease of the impact angle at the impact angles <30° for the porous gypsum targets and <55° for the glass targets. Therefore, when we determine the impact strength for an impact angle smaller than these critical angles, θ_c, it can be expected to be >1000 J kg^{-1}. It should thus be considered how the impact angle affects the impact strength and what types of physical mechanisms control the impact strength for an oblique impact. We can then reanalyze the impact strength by using the effective specific

energy, Q_{eff}, which is defined by the following equation:

$$Q_{\mathrm{eff}} = Q \sin^2 \theta = \frac{\frac{1}{2} m_{\mathrm{p}} (v_{\mathrm{i}} \sin \theta)^2}{M_{\mathrm{t}} + m_{\mathrm{p}}}. \quad (3)$$

The velocity component normal to the impact surface, $v_{\mathrm{i}} \sin \theta$, is only introduced into the specific energy in Eq. (3) because we assume that it could induce mainly the impact pressure and thereby contribute to the damage to the entire target [*Chapman and McKinnon*, 1986; *Pierazzo and Melosh*, 2000]. We next examine the relationship between the NLFM and the Q_{eff} in order to discuss the effect of the impact angle on the impact strength.

This relationship (for both types of target) is illustrated in Fig. 13. Although the data are slightly scattered, they were almost consistent with each other, and were fitted by one empirical equation at the NLFM values <0.75, irrespective of the impact angle. However, the NLFM of the glass targets behaved differently compared to that of the porous gypsum targets (Fig. 13a, b). The empirical equation obtained below $m_{\mathrm{l}}/M_{\mathrm{t}}$= 0.75 for the porous gypsum targets could be simply extrapolated until unity, and it was well consistent with the NLFM values >0.75, whereas the two empirical equations below and above $m_{\mathrm{l}}/M_{\mathrm{t}}$= 0.75 for the glass targets were clearly necessary. It is clear for glass targets at $m_{\mathrm{l}}/M_{\mathrm{t}}$

Fig. 13

>0.75 that the NLFM gradually decreased with the increase of the Q_{eff}, and the target appeared to be a sphere truncated at both the impact and antipodal points as shown in Fig. 9a–c. At $m_{\mathrm{l}}/M_{\mathrm{t}}$ <0.75, the NLFM greatly decreased with the increase of the Q_{eff}, and the target was catastrophically disrupted (Fig. 9d–f).

We can write the empirical equation representing the relationship between the NLFM and the Q_{eff} for both targets in the form of a power law equation:

$$\frac{m_{\mathrm{l}}}{M_{\mathrm{t}}} = 10^{p_2} \cdot {Q_{\mathrm{eff}}}^{-q_2}. \qquad (4)$$

The parameters p_2 and q_2 are summarized in Table 4, and we note that two empirical equations with different p_2 and q_2 values were necessary for glass targets at the NLFM values >0.75 and at those <0.75. By using these empirical equations, we were able to obtain the effective impact strength, ${Q_{\mathrm{eff}}}^*$, defined as the effective specific energy when the NLFM was equal to 0.5, and the obtained ${Q_{\mathrm{eff}}}^*$ values are also shown in Table 4. Surprisingly, the ${Q_{\mathrm{eff}}}^*$ for both targets were very similar to 1000 J kg^{-1} derived from the head-on collision. Thus, this similarity may support our assumption that the velocity component normal to the impact surface was mainly responsible for the impact pressure that damaged the entire target in the oblique impact. We can then recalculate the impact

Table 4

strength Q^* by using the effective impact strength $Q_{\mathrm{eff}}{}^*$ at various impact angles, since the results of our experiments confirmed that $Q_{\mathrm{eff}}{}^*$ can be written as $Q^* \sin^2 \theta$.

The results of the porous gypsum and glass targets are shown together in Fig. 13c. It can be easily seen that the NLFM for the porous gypsum targets was always larger than that for the glass targets over the range of Q_{eff} explored in these experiments, and the NLFM of both targets crossed at Q_{eff} = 750 J kg^{-1} and $m_{\mathrm{l}}/M_{\mathrm{t}}$ = 0.69. The results for basalt obtained by *Fujiwara and Tsukamoto* [1980] are also shown in Fig. 13c; they carried out impact experiments for a basalt sphere or cube at impact angles from 90° to 30° and the impact velocity of approximately 2.7 km s^{-1}. The parameters p_2 and q_2 and the effective impact strength $Q_{\mathrm{eff}}{}^*$ of their basalt targets are also shown in Table 4 for a comparison with our findings. The NLFM of basalt was well consistent with that of our glass targets.

To test whether the empirical equation, Eq. (4), can reproduce the relationship between the NLFM and the impact angle θ, we prepared Fig. 14 illustrating the relationship between the NLFM and the $\sin\theta$ values and replotted our data in the figure. Equation (4) with the p_2 and q_2 data shown in Table 4 was then drawn. It was thus

Fig. 14

clear that Eq. (4) could reproduce our experimental results very well for both types of targets, although the glass target results were slightly scattered for 1000 J kg^{-1} and at the $\sin\theta$ values >0.8, as shown in Fig. 14b.

We reanalyzed the antipodal velocity, V_{a}, for the porous gypsum targets by using the Q_{eff} to examine the effects of the impact angle on the V_{a}. This relationship is illustrated in Fig. 15a. As with the NLFM results, the V_{a} results were well merged and fitted by the following empirical equation:

Fig. 15

$$V_{\mathrm{a}} = 10^{-1.72\pm0.10} {Q_{\mathrm{eff}}}^{0.68\pm0.03}. \qquad (5)$$

As shown in Fig. 15b, we were also able to reproduce the relationship between the V_{a} and the specific energy for porous gypsum targets by using Eq. (5), and the data shown in Fig. 6 were also replotted. The use of Eq. (5) clearly reproduced our experimental results very well, as with the results of Fig. 14. We were thus also able to recalculate the antipodal velocity V_{a} by using Eq. (5) at various impact angles.

4.2. Implications for the probability of impact disruption considering oblique impacts

Our findings clarified that the degree of disruption represented by the NLFM depends

on the impact angle for porous gypsum and glass targets, as described in Eq. (4). The probability of an impact at an impact angle between θ and $\theta + d\theta$ is described as $dP = 2\sin\theta\cos\theta\, d\theta$ according to *Shoemaker* [1962] and *Pierazzo and Melosh* [2000], irrespective of the target body's gravity. In the following discussion, therefore, we will consider the effects of the probability of oblique impacts on the degree of disruption in the solar nebula, and we speculate that (1) primitive rocky planetesimals could be represented by our porous gypsum targets, and (2) consolidated rocky planetesimals could be represented by our glass targets.

The probability density function for oblique impacts is expressed as:

$$\frac{dP}{d\theta} = 2\sin\theta\cos\theta, \qquad (6)$$

and this function has the maximum at $\theta = 45°$. By using Eqs. (3), (4), and (6), we can obtain the relationship between the probability density function, $dP/d\theta$, and the normalized largest fragment mass (NLFM), $m_\mathrm{l}/M_\mathrm{t}$, as follows:

$$\frac{dP}{d\theta} = 2\left[k^{-1}\left(\frac{2m_\mathrm{l}}{M_\mathrm{t}}\right)^{-\frac{1}{q_2}}\left\{1 - k^{-1}\left(\frac{2m_\mathrm{l}}{M_\mathrm{t}}\right)^{-\frac{1}{q_2}}\right\}\right]^{\frac{1}{2}}, \qquad (7)$$

where k represents the specific energy normalized by the impact strength, Q/Q^*, and $Q_\mathrm{eff}{}^*$ was assumed to be equal to Q^* based on our present findings. The detailed

derivation process considered by Eq. (7) is explained in the Appendix. The relationship between the $dP/d\theta$ and the NLFM can be calculated at various specific energies in Eq. (7), and it can then be estimated how oblique impacts in the solar nebula affected the NLFM, because it was clear according to Eq. (6) that almost no head-on collisions occurred; a specific energy larger than Q^* was therefore necessary to cause a catastrophic disruption in the planetary collisional processes considering the oblique impacts.

Fig. 16a shows the relationship between the $dP/d\theta$ and m_l/M_t data for primitive rocky planetesimals simulated by porous gypsum. The function is calculated for the normalized specific energy of $k = 3$ ($Q^* = 1.33 \times 10^3$ J kg^{-1} and $q_2 = 0.76$). The $dP/d\theta$ increases with increasing m_l/M_t, reaches a maximum of $dP/d\theta = 1$ at $m_l/M_t = 0.37$, and then decreases with increasing m_l/M_t to become $dP/d\theta = 0.68$ at $m_l/M_t = 1$. The numbers added to the function of $dP/d\theta$ show the impact angle corresponding to each m_l/M_t, and the results demonstrate that the probability density function is 0 at $\theta = 90°$ and 1 (the maximum) at $\theta = 45°$. Moreover, the m_l/M_t is 1 at the θ of 21.5°; this means that the planetesimals were almost intact when they were

Fig. 16

impacted at an impact angle ≤21.5°.

The cumulative distribution function, $P(<\theta)$, is also shown in Fig. 16a. We define the $P(<\theta)$ as the impact probability, i.e., it indicates the probability of impact at an impact angle smaller than a specific impact angle θ. The $P(<\theta)$ can be obtained by integrating Eq. (7) with respect to the impact angle θ from 0° to a specific θ, and the $m_{\mathrm{l}}/M_{\mathrm{t}}$ corresponding to each impact angle is calculated by using Eqs. (3) and (4) at constant k; the relationship between $P(<\theta)$ and $m_{\mathrm{l}}/M_{\mathrm{t}}$ is then derived as shown in Fig. 16a. It is observed that the $m_{\mathrm{l}}/M_{\mathrm{t}}$ is ≥0.37 with a probability of 50%, and the planetesimals are almost intact with a probability of 14%.

Fig. 16b shows the impact probability for primitive and consolidated rocky planetesimals, which were calculated for the normalized specific energy k of 0.7, 1, 3, and 10. We used the parameters of porous gypsum and glass targets listed in Table 4 to calculate these values. In both planetesimals, the $m_{\mathrm{l}}/M_{\mathrm{t}}$ becomes smaller with the increase of the normalized specific energy at the same impact probability. It was also shown that at $m_{\mathrm{l}}/M_{\mathrm{t}} = 1$, the impact probability corresponding to keeping planetesimals intact after the collision decreases with the increase of the normalized specific energy. In

comparison of the results of the primitive rocky planetesimals with those of the consolidated planetesimals, the degree of disruption (m_l/M_t) for the consolidated rocky planetesimals fluctuated approximately four times at the impact probability between the head-on collision ($P = 1$) and the oblique impact of 45° ($P = 0.5$), whereas the m_l/M_t of the primitive rocky planetesimals was almost constant within the same impact probability range.

At the same normalized specific energy, the impact probability of the primitive rocky planetesimals for m_l/M_t <0.5 is always larger than that of the consolidated rocky planetesimals. For example, at the normalized specific energy of 10, the impact probability of the primitive rocky planetesimals for m_l/M_t >0.1 is 0.83 (θ ~66°) and that of the consolidated rocky planetesimals is 0.27 (θ ~31°). Thus there is a more than threefold difference in the impact probability between them. As a result, the consolidated rocky planetesimals can be more easily disrupted into small fragments compared to the primitive rocky planetesimals.

In contrast, the impact probability of the consolidated rocky planetesimals is larger than that of the primitive rocky planetesimals for m_l/M_t >0.5 at the same k. It is also

notable that the impact probability for both planetesimals crosses at $m_l/M_t = 0.5$ when the k is the same. In this case, the impact angle can be determined by using the following equation, $\theta_{CD} = \arcsin(k^{-1/2})$, from $Q_{eff} = Q\sin^2\theta$ and the assumption of $Q_{eff}{}^* = Q^*$. That is, the impact angle at which the catastrophic disruption could begin to occur, θ_{CD}, is independent of the target material, but it depends only on the specific energy normalized by the impact strength. At a θ larger than the θ_{CD}, the target body could be disrupted catastrophically, and we can thus calculate the range of the θ necessary for catastrophic disruption at each k.

According to this θ range, we can also calculate the impact probability of rocky planetesimals at catastrophic disruption in the solar nebula by using Eq. (6), as $P(>\theta) = 1 - k^{-1}$. Fig. 16c describes the relationship between the impact probability $P(>\theta)$ corresponding to the occurrence of catastrophic disruption, and the normalized specific energy k. The impact probability $P(>\theta)$ at the NLFM <0.5 increased with the increase of the k, and it was closer to unity at large k values. That is, the catastrophic disruption could occur even at a low impact angle as the normalized specific energy increases. For example, to be necessary for catastrophic disruption with a probability of 50% (θ =90°–

45°), $k = 2$ is proposed, and for a probability of 75% (θ =90°–30°), $k = 4$ is proposed. We can therefore say that the catastrophic disruption could have occurred at a wide range of impact angles when the specific energy at the collision was approximately four times larger than the impact strength.

The effects of oblique impacts described in this study should thus be considered in order to construct the appropriate numerical model for the study of the mass frequency distributions of planetesimals and asteroids.

In this study, we examined the collisional disruption of solid materials in a strength-dominated regime. Our experimental results can be applied to mutual collisions of bodies with a radius <100 m in a strength regime [*Holsapple et al.*, 2002]. However, to apply our experimental results to the collisional disruption of asteroids and planetesimals >100 m, the effect of the bodies' self-gravity on the re-accumulation processes of impact fragments should be considered. In this study, we provide the basic data of the ejecta velocity distribution and the mass distributions of impact fragments that are necessary for the study of re-accumulation processes of the bodies. Numerical simulations referring to our experimental results are expected in the future.

5. Summary

We carried out oblique high-velocity impact experiments using porous gypsum and glass spheres at impact angles from 90° (a head-on collision) to 10° (a grazing collision) and at impact velocities from 7 to 2 km s^{-1}. We then examined the effects of the impact angle on the ejection velocity of the impact fragments and the impact strength. Our results are summarized as follows:

(1) The expanding velocity of the ejecta envelope was measured. At the initial position angle of 0° (the antipodal point), the expanding velocity became the minimum at a head-on collision for the porous gypsum targets. As the impact angle decreased, the initial position angle where the expanding velocity showed the minimum changed from 0° to +30° . For the glass targets, in contrast, the expanding velocity reached the maximum at the initial position angle of 0°, irrespective of the impact angle.

(2) When the Q was constant, the NLFM, $m_{\mathrm{l}}/M_{\mathrm{t}}$, was almost the same at the large impact angle, whereas it rose markedly with the decrease of the impact angle at θ values smaller than 30° and 55° for the porous gypsum and glass targets, respectively.

The impact strength Q^* values for the porous gypsum and glass targets at a head-on collision were obtained to be 1330 and 1070 J kg^{-1}, but compared to the porous gypsum targets, the glass targets were disrupted more catastrophically with a small change of the specific energy.

(3) We defined the effective specific energy, Q_{eff} $(= Q \sin^2 \theta)$, and observed that the NLFM, $m_{\mathrm{l}}/M_{\mathrm{t}}$, had a good correlation with the Q_{eff} irrespective of the impact angle. At the $m_{\mathrm{l}}/M_{\mathrm{t}}$ values <0.75, the relationship can be written as $m_{\mathrm{l}}/M_{\mathrm{t}} = 10^{2.02\pm0.22} \cdot {Q_{\mathrm{eff}}}^{-0.76\pm0.06}$ for the porous gypsum targets and $m_{\mathrm{l}}/M_{\mathrm{t}} = 10^{4.66\pm0.39} \cdot {Q_{\mathrm{eff}}}^{-1.68\pm0.12}$ for the glass targets. The effective impact strength ${Q_{\mathrm{eff}}}^*$, i.e., the Q_{eff} at $m_{\mathrm{l}}/M_{\mathrm{t}}$ =0.5, was surprisingly consistent for both types of target at ~1000 J kg^{-1}. The relationship between the antipodal velocity for the porous gypsum targets V_{a} and the Q_{eff} was obtained as $V_{\mathrm{a}} = 10^{-1.72\pm0.10} {Q_{\mathrm{eff}}}^{0.68\pm0.03}$.

(4) We estimated the relationship between the impact probability and the NLFM, $m_{\mathrm{l}}/M_{\mathrm{t}}$, by using our empirical equations. At the $m_{\mathrm{l}}/M_{\mathrm{t}}$ <0.5, the impact probability of consolidated rocky planetesimals simulated by glass targets was always smaller than that of primitive rocky planetesimals simulated by porous gypsum targets at a constant

normalized specific energy Q/Q^*, while these results were the opposite at the m_l/M_t >0.5. Our findings also clarified that catastrophic disruption can occur at an impact angle from 30° to 90° irrespective of the target materials when the specific energy at the collision is approximately four times larger than the impact strength.

Appendix

The probability density function of impacting bodies, $dP/d\theta$, shown by Eq. (6) can be rearranged as

$$\frac{dP}{d\theta} = 2\sin\theta\cos\theta = 2\sin\theta\,(1-\sin^2\theta)^{\frac{1}{2}}, \qquad \text{(A1)}$$

by using the fundamental Pythagorean trigonometric identity.

By using Eqs. (3) and (4), we can obtain the relationship between the specific energy Q and $\sin\theta$ as follows:

$$\sin\theta = \left[\frac{1}{Q}\left\{\frac{1}{A'}\left(\frac{m_\mathrm{l}}{M_\mathrm{t}}\right)\right\}^{-\frac{1}{q_2}}\right]^{\frac{1}{2}}, \qquad \text{(A2)}$$

where $A' = 10^{p_2}$. Thus, substituting Eq. (A2) for Eq. (A1), we have

$$\frac{dP}{d\theta} = 2\left[\frac{1}{Q}\left\{\frac{1}{A'}\left(\frac{m_\mathrm{l}}{M_\mathrm{t}}\right)\right\}^{-\frac{1}{q_2}}\right]^{\frac{1}{2}}\left(1-\left[\frac{1}{Q}\left\{\frac{1}{A'}\left(\frac{m_\mathrm{l}}{M_\mathrm{t}}\right)\right\}^{-\frac{1}{q_2}}\right]\right)^{\frac{1}{2}}. \qquad \text{(A3)}$$

Here, we assumed that the effective impact strength ${Q_\mathrm{eff}}^*$ was equal to the impact strength Q^* when the NLFM was 0.5, as described in Section 4.2. We can thus obtain the Q^* by using Eq. (4) as follows:

$$\left(\frac{1}{A'}\right)^{-\frac{1}{q_2}} = 2^{-\frac{1}{q_2}}\cdot Q^*. \qquad \text{(A4)}$$

Thus, substituting Eq. (A4) for Eq. (A3), we can obtain Eq. (7).

Acknowledgements

We appreciate the assistance of Dr. K. Ogawa and Dr. C. Okamoto of Kobe University in the conduct of these experiments. We also thank Mr. K. Sangen of Kobe University for his technical help. Our series of our experiments were supported in part by the Center of Planetary Science at Kobe University and the Hypervelocity Impact Facility at ISAS/JAXA. This work was supported in part by a Grant-in-Aid for Scientific Research (no. 16H04041) from the Japan Ministry of Education, Culture, Sports, Science and Technology.

References

Arakawa, M., 1999a. Ejection velocities of ice fragments in oblique impacts of ice spheres. Adv. Space Res. 23, 1217–1224.

Arakawa, M., 1999b. Collisional disruption of ice by high-velocity impact. Icarus 142, 34–45.

Arakawa, M., Leliwa-Kopystynski, J., Maeno, N., 2002. Impact experiments on porous icy-silicate cylindrical blocks and the implication for disruption and accumulation of

small icy bodies. Icarus 158, 516–531.

Ashby, M. F., 2013. Material profiles. In: Materials and the Environment 2nd Edition, Elsevier, pp. 459–595.

Asphaug, E., Ryan, E. V., Zuber, M. T., 2002. Asteroid interiors. In: Asteroids III, Eds: Bottke, W. F., Cellino, A., Paolicchi, P., Binzel, R., Univ. Arizona Press, Tucson, pp. 463–484.

Chapman, C. R., McKinnon, W. B., 1986. Cratering of planetary satellites. In *Satellites,* eds: J. A. Burns, M. S. Matthews, Univ. Arizona Press, Tucson, pp. 492–580.

Fujii, Y., Nakamura, A. M., 2009. Compaction and fragmentation of porous gypsum targets from low-velocity impacts. Icarus 201, 795–801.

Fujiwara, A., Kamimoto, G., Tsukamoto, A., 1977. Destruction of basaltic bodies by high-velocity impact. Icarus 31, 277–288.

Fujiwara, A., Tsukamoto, A., 1980. Experimental study on the velocity of fragments in collisional breakup. Icarus 44, 142–153.

Gault, D. E., Wedekind. J. A., 1969. The destruction of tektites by micrometeoroid impact. J. Geophys. Res. 74, 6780–6794.

Genda, H., Fujita, T., Kobayashi, H., Tanaka, H., Suetsugu, R., Abe, Y., 2017. Impact erosion model for gravity-dominated planetesimals. Icarus 294, 234–246.

Heißelmann, D., Blum, J., Fraser, H. J., and Wolling, K., 2010. Microgravity experiments on the collisional behavior of saturnian ring particles. Icarus 206, 424–430.

Henke, S., Gail, H.-P., Trieloff, M., Schwarz, W. H., Kleine, T., 2012. Thermal evolution and sintering of chondritic planetesimals. Astron. Astrophys. 537, A45.

Holsapple, K. A., Giblin, I., Housen, K. R., Nakamura, A., Ryan, E., 2002. Asteroid impacts: Laboratory experiments and scaling laws. In Asteroids III, eds: W. F. Bottke Jr., A. Cellino, P. Paolicchi, R. P. Binzel, Univ. Arizona Press, Tucson, pp. 443–462.

Kadono, T., Arakawa, M., Ito, T., Ohtsuki, K., 2009. Spin rates of fast-rotating asteroids and fragments in impact disruption. Icarus 200, 694–697.

Kawakami, S., Mizutani, H., Takagi, Y., Kato, M., Kumazawa, M., 1983. Impact experiments on ice. J. Geophys. Res. 88, 5806–5814.

Kawakami, S., Kanaori, Y., Fujiwara, A., Arakawa, M., Kato, M., Mizutani, H., Cerroni, P., Capaccioni, F., 1991. An experimental study of impact fracturing of small planetary bodies in the solar system with an application to Phobos. Astronom.

Astophys. 241, 233–242.

Leinhardt, Z. M., Richardson, D. C., 2002. *N*-Body simulations of planetesimal evolution: Effect of varying impactor mass ratio. Icarus 159, 306–313.

Lichtenberg, T., Golabek, G. J., Gerya, T. V., Meyer, M. R., 2016. The effects of short-lived radionuclides and porosity on the early thermo-mechanical evolution of planetesimals. Icarus 274, 350–365.

Love, S. G., Hörz, F., Brownlee, D. E., 1993. Target porosity effects in impact cratering and collisional disruption. Icarus 105, 216–224.

Melosh, H. J., 1989. Impact cratering. Oxford Univ. Press, New York, pp. 245.

Morris, A. J. W., Burchell, M. J., 2017. Laboratory tests of catastrophic disruption of rotating bodies. Icarus 296, 1–98.

Movshovitz, N., Nimmo, F., Korycansky, D. G., Asphaug, E., Owen, J. M., 2016. Impact disruption of gravity-dominated bodies: New simulation data and scaling. Icarus 275, 85–96.

Nakamura, A. M., 1993. Laboratory studies on the velocity of fragments from impact disruptions. The institute of Space and Astronautical Science Report, No. 651, ISSN

0285–6808.

Nakamura, A. M., Hiraoka, K., Yamashita, Y., Machii, N., 2009. Collisional disruption experiments of porous targets. Planet. Space Sci. 57, 111–118.

Neumann, W., Breuer, D., Spohn, T., 2012. Differentiation and core formation in accreting planetesimals. Astron. Astrophys. 543, A141.

Okamoto, C., Arakawa, M., 2009. Experimental study on the collisional disruption of porous gypsum spheres. Meteorit. Planet. Sci. 44, 1947–1954.

Onose, N., Fujiwara, A., 2004. Mass-velocity distributions of fragments in oblique impact cratering on gypsum. Meteorit. Planet. Sci. 39, 321–331.

Paolicchi, P., Cellino, A., Farinella, P., Zappala, V., 1989. A semiempirical model of catastrophic breakup processes. Icarus 77, 187–212.

Pierazzo, E., Melosh, H. J., 2000. Understanding oblique impacts from experiments, observations, and modeling. Annu. Rev. Earth Planet. Sci. 28, 141–167.

Shoemaker, E. M., 1962. Interpretation of lunar craters. In: Kopal, Z. (Ed.), Physics and astronomy of the Moon. New York: Academic Press, pp. 283–359.

Sierks H. et al., 2011. Images of Asteroid 21 Lutetia: A remnant planetesimal from the

early solar system. Science 334, 487–490.

Takagi, Y., Mizutani, H., Kawakami, S., 1984. Impact fragmentation experiments of basalts and pyrophyllites. Icarus 59, 462–477.

Weidenschilling, S. J., 1994. Origin of cometary nuclei as ‘rubble piles’. Nature 368, 721–723.

Weidenschilling, S. J., 2011. Initial sizes of planetesimals and accretion of the asteroids. Icarus 214, 671–684.

Yasui, M., Arakawa, M., 2011. Impact experiments of porous gypsum-glass bead mixtures simulating parent bodies of ordinary chondrites: Implications for re-accumulation processes related to rubble-pile formation. Icarus 214, 754–765.

Yasui, M., Arakawa, M., Hasegawa, S., Fujita, Y., Kadono, T., 2012. In situ flash X-ray observation of projectile penetration processes and crater cavity growth in porous gypsum target analogous to low-density asteroids. Icarus 221, 646–657.

Figure Captions

Figure 1:

Top view of the two-stage light gas gun and experimental setup. The small panel at upper right provides a side view of the recovery box.

Figure 2:

The analysis method used to determine the impact angle, θ. (a) Definition of the θ. (b) Example of the θ determined by using the images taken by a shutter camera. Left images were taken at 5 and 12 μs before the impact. Right image is the superimposed image by using two images on the left. (c) Example of the θ determined by using the images taken by a high-speed camera. The images are the identical, but some notes are added on the right image to determine the impact angle. The impact point was determined as the middle point on the line linking both ejecta necks.

Figure 3:

Snapshots of the porous gypsum targets taken by the high-speed camera. The run number and the impact angle in each panel were as follows. (a) 20141208-1, θ=75°. (b) 20141209-2, θ=45°. (c) 20150515-1, θ=10°. (d) 20150515-2, θ=90°. (e) 20150515-3, θ=55°. (f) 20151119-3, θ=15°. The specific energy in each figure was 3×10^3 J kg^{-1} in (a–c) and 10^4 J kg^{-1} in (d–f). The black circle represents the projectile and the arrow represents the projectile trajectory. The black bar shown on each panel represents a length of 10 mm. The number shown on the right of each image represents the elapsed time after the impact in ms, and "0 ms" indicates the moment of impact.

Figure 4:

Snapshots of the glass targets taken by the high-speed camera. The run number and the impact angle in each panel were as follows. (a) 20151007-1, θ=80°. (b) 20151008-2, θ=45°. (c) 20151125-1, θ=15°. (d) 20151001-1, θ=80°. (e) 20151118-1, θ=40°. (f) 20151202-1, θ=15°. The specific energy in each figure was 10^3 J kg^{-1} in (a–c) and 4×10^3 J kg^{-1} in (d–f). The black circle represents the projectile and the arrow represents the projectile trajectory. The black bar shown on each panel represents a length of 10 mm.

The number shown on the right of each image represents the elapsed time after the impact in ms, and "0 ms" indicates the moment of impact. The fifth image on panel (c) was taken at 15 ms after the impact.

Figure 5:

(a) Schematic illustration of the definition of the initial position angle. (b) Relationship between the expanding velocity of the ejecta envelope and the initial position angle for the porous gypsum targets at the specific energy of 10^4 J kg^{-1}. The run numbers of all data are shown in Table 1. The numbers in the legend indicate the measured impact angle and those in parentheses indicate the impact angle used in the text. (c) Relationship between the expanding velocity and the initial position angle for the glass targets at the specific energy of 4×10^3 J kg^{-1}. The run numbers of all data are shown in Table 2. (d) The enlarged part of the vertical axis in panel (c) ranging from 0 m s^{-1} to 50 m s^{-1}. The error bars on panels (b) – (d) were smaller than the symbol's size.

Figure 6:

Relationship between the antipodal velocity V_a and the specific energy Q for the porous gypsum targets. Each symbol represents the impact angle. The dashed thick line represents the fitting line determined by using the power law equation of Eq. (1). Four thin lines show the results for H_2O ice, basalt, and porous gypsum obtained in previous works. The numbers in the parentheses indicate the impact angle: "ice" obtained by *Arakawa* [1999a], "basalt" by *Fujiwara and Tsukamoto* [1980], and "gypsum" by *Okamoto and Arakawa* [2009].

Figure 7:

Relationship between the antipodal jet velocity V_{jet} and the specific energy Q for the glass targets. The symbols represent different impact angles.

Figure 8:

Photographs of the recovered impact fragments of the porous gypsum targets at the specific energy of 3×10^3 J kg^{-1} in (a–c) and at 10^4 J kg^{-1} in (d–f). The run number and the impact angle in each panel were as follows. (a) 20141208-1, θ=75°. (b) 20141209-2,

θ=45°. (c) 20150515-1, θ=10°. (d) 20141209-5, θ=75°. (e) 20141209-7, θ=40°. (f) 20150722-1, θ=15°. ”LF” surrounded by the white dashed line was the largest fragment. The fragment shown on panels (c) and (f) is the largest.

Figure 9:

Photographs of the recovered impact fragments of the glass targets at the specific energy of 10^3 J kg^{-1} in (a–c) and at 4×10^4 J kg^{-1} in (d–f). The run number and the impact angle in each panel were as follows. (a) 20151007-1, θ=80°. (b) 20151028-2, θ=40°. (c) 20151125-1, θ=15°. (d) 20151001-1, θ=80°. (e) 20151118-1, θ=40°. (f) 20151202-1, θ=15°. ”LF” surrounded by the white dashed line was the largest fragment. The small boxes in (a–c) are expanded images of the largest fragment in each panel.

Figure 10:

Mass frequency distributions of recovered impact fragments for (a) the porous gypsum targets at the specific energy of 3×10^3 J kg^{-1} and (b) the glass targets at the specific energy of 4×10^3 J kg^{-1}. Each symbol represents the impact angle. The numbers in the

legend indicate the measured impact angle. The numbers in parentheses indicate the impact angle used in the text. (c) Relationship between the power law index α in the power law equation showing the mass frequency distribution of impact fragments and the impact angle. The solid line and dashed line show the average values of α for the porous gypsum and glass targets, respectively.

Figure 11:

Relationship between the largest fragment mass normalized by the original target mass (NLFM), $m_{\mathrm{l}}/M_{\mathrm{t}}$, and the impact angle θ for (a) the porous gypsum targets and (b) the glass targets. The numbers in the legend represent the target diameter and the impact velocity. The numbers in the parentheses indicate the specific energy. The dashed line indicates the critical impact angle of the quasi-constant NLFM, θ_{c}.

Figure 12:

Relationship between the largest fragment mass normalized by the original target mass (NLFM), $m_{\mathrm{l}}/M_{\mathrm{t}}$, and the specific energy Q for (a) the porous gypsum targets and (b)

the glass targets. Each symbol represents the impact angle. The solid line shows the fitting line determined by using the power law equation of Eq. (2) at the impact angle of 90° and 80°. The dotted line indicates the previous results for porous gypsum obtained by *Okamoto and Arakawa* [2009] shown as "O&A [2009]" on panel (a) and for basalt obtained by *Fujiwara and Tsukamoto* [1980] shown as "F&T [1980]" on panel (b).

Figure 13:

Relationship between the largest fragment mass normalized by the original target mass (NLFM), $m_{\mathrm{l}}/M_{\mathrm{t}}$, and the effective specific energy Q_{eff} defined by Eq. (3), for (a) the porous gypsum targets and (b) the glass targets. Each symbol represents the impact angle. The solid line shows the fitting line determined by using the power law equation of Eq. (4). (c) The merged figure of panels (a) and (b) and the previous results for basalt obtained by *Fujiwara and Tsukamoto* [1980] shown as "F&T, 1980". Three lines show the fitting lines determined by using Eq. (4).

Figure 14:

Relationship between the largest fragment mass normalized by the original target mass (NLFM), $m_{\mathrm{l}}/M_{\mathrm{t}}$, and the $\sin\theta$ (the θ is the impact angle) for (a) the porous gypsum targets and (b) the glass targets. Each symbol represents the experimental results, and the numbers in the legend represent the target diameter and the impact velocity. The thick lines show the calculated results from Eq. (4) with the obtained parameters in Table 4 at each specific energy.

Figure 15:

(a) Relationship between the antipodal velocity V_{a} and the effective specific energy Q_{eff} for the porous gypsum targets. Each symbol represents the impact angle. The thick solid line shows the fitting line determined by using the power law equation of Eq. (5). (b) Relationship between the antipodal velocity V_{a} and the specific energy Q. The data plotted in this figure are identical to those in Fig. 6. The thick solid line shows the fitting line by using Eq. (1). The thin lines show the calculated results from Eq. (5) at impact angles of 45° (short dashed line), 30° (long dashed line), 20° (thin solid line), and 15° (dotted line).

Figure 16:

(a) Relationship between the probability density function of an impact, $dP/d\theta$ (solid line) on the left vertical axis, or the impact probability, $P\ (< \theta)$ (thick dotted line) on the right vertical axis, and the normalized largest fragment mass (NLFM), $m_{\mathrm{l}}/M_{\mathrm{t}}$, for a primitive planetesimal simulated by porous gypsum at the specific energy normalized by the impact strength Q/Q^* of 3. The number on the solid line shows the impact angle θ corresponding to each NLFM. The two circle symbols on the thick dotted line show the data at $P =$ 0.5 and $\theta =$ 45°, and that at $P =$ 0.14 and $m_{\mathrm{l}}/M_{\mathrm{t}} =$ 1. (b) Relationship between the impact probability $P\ (< \theta)$ and the NLFM, $m_{\mathrm{l}}/M_{\mathrm{t}}$, at the normalized specific energy $Q/Q^*\ (= k)$ of 0.7, 1, 3, and 10 for a primitive planetesimal and a consolidated planetesimal simulated by porous gypsum and glass, respectively. The solid grey line indicates $m_{\mathrm{l}}/M_{\mathrm{t}}$ =0.5. The two circles show the data at $P =$ 0.83 on the thin dashed line (primitive planetesimal) and $P =$ 0.27 on the thick dashed line (consolidated planetesimal) at $m_{\mathrm{l}}/M_{\mathrm{t}} =$ 0.1 and $k = 10$. (c) Relationship between the impact probability $P(> \theta)$, corresponding to the occurrence of catastrophic disruption (the

NLFM, $m_{\mathrm{l}}/M_{\mathrm{t}}$ <0.5), and the k. The number near each circle on the line shows the impact angle θ corresponding to each k.

Table 1. Experimental conditions and results for porous gypsum targets

Run number [a]	Target			Impact velocity v_i, km s^{-1}	Impact angle θ^b, degree	Specific energy Q, J kg^{-1}	NLFM $m_l/M_t{}^c$	Antipodal velocity $V_a{}^d$, m s^{-1}	α^e
	Mass M_t, g	Diameter, mm	Porosity, %						
Oblique impact: Target diameter = 70 mm, Impact velocity ~3.8 km s^{-1}									
20141208-1$^+$	180.3	70.1	54	3.66	77.8 (75)	2.51 x 10^3	0.341	3.27 (0.09)	0.58 (0.02)
20141208-2	171.1	69.8	56	3.73	74.9 (75)	2.76 x 10^3	0.283	3.14 (0.09)	0.67 (0.03)
20141209-1	161.3	69.1	58	3.74	53.7 (55)	2.94 x 10^3	0.415	2.67 (0.06)	0.72 (0.01)
20141209-2$^+$	171.4	69.3	55	3.80	43.4 (45)	2.86 x 10^3	0.417	2.37 (0.04)	0.68 (0.02)
20141209-3$^+$	174.8	69.8	55	3.74	27.6 (30)	2.71 x 10^3	0.865	1.40 (0.02)	0.77 (0.03)
20150114-3	150.5	69.9	62	3.78	12.0 (10)	3.22 x 10^3	0.997	–	0.80 (0.05)
20150515-1$^+$	162.8	70.1	59	3.78	9.2 (10)	2.98 x 10^3	0.994	0.43 (0.01)	0.76 (0.09)
Oblique impact: Target diameter = 50 mm, Impact velocity ~3.8 km s^{-1}									
20150515-3*	50.5	48.9	63	3.76	55.9 (55)	9.49 x 10^3	0.144	9.86 (0.04)	0.86 (0.01)
20150515-4*	48.9	49.3	64	3.84	21.5 (20)	1.02 x 10^4	0.205	4.55(0.09)	0.87 (0.01)
20151119-3*	53.4	48.5	59	4.07	14.9 (15)	1.05 x 10^4	0.582	1.78 (0.03)	–
Oblique impact: Target diameter = 70 mm, Impact velocity ~6.9 km s^{-1}									
20141209-5	174.6	70.1	56	6.94	78.0 (75)	9.36 x 10^3	0.116	7.74 (0.08)	0.71 (0.01)
20141209-6	176.7	69.6	55	6.98	58.8 (60)	9.35 x 10^3	0.214	7.87 (0.12)	0.65 (0.01)
20141209-7	177.8	69.4	54	6.88	41.4 (40)	9.03 x 10^3	0.221	7.22 (0.23)	0.71 (0.01)
20150721-1	175.5	69.2	54	6.91	42.0 (40)	9.25 x 10^3	0.276	–	0.78 (0.02)
20150721-2	145.3	69.2	62	7.06	38.5 (40)	1.16 x 10^4	0.224	–	–
20151119-4	152.6	68.9	59	6.90	32.1 (30)	1.06 x 10^4	0.179	4.51 (0.07)	–
20150722-1	174.9	69.6	55	6.83	13.8 (15)	9.06 x 10^3	0.995	–	–

Table 1. Continued

Run number [a]	Target			Impact velocity v_i, km s^{-1}	Impact angle θ[b], degree	Specific energy Q, J kg^{-1}	NLFM m_l/M_t[c]	Antipodal velocity V_a[d], m s^{-1}	α[e]
	Mass M_t, g	Diameter, mm	Porosity, %						
Head-on collision									
20161213-1	200.4	69.7	49	3.02	82.0 (80)	1.55 x 10^3	0.669	2.26 (0.004)	0.69 (0.03)
20161220-1	120.7	58.9	49	3.08	82.7 (80)	2.67 x 10^3	0.287	3.88 (0.04)	0.68 (0.01)
20161220-2	70.1	49.3	49	3.14	80.9 (80)	4.76 x 10^3	0.227	7.10 (0.16)	0.74 (0.02)
20170110-1	37.2	39.5	48	3.19	90.0 (90)	9.27 x 10^3	0.090	13.80 (0.22)	0.77 (0.04)
20150715-1	84.1	59.0	65	3.73	83.4 (80)	5.64 x 10^3	0.151	6.80 (0.02)	–
20150515-2*	50.3	49.2	63	3.74	88.7 (90)	9.43 x 10^3	0.109	9.98 (0.08)	0.86 (0.02)
20150715-2	27.4	40.3	64	3.83	81.6 (80)	1.81 x 10^4	0.054	16.27 (0.09)	–
20161011-1	202.0	70.3	50	4.04	85.3 (90)	2.75 x 10^3	0.181	3.58 (0.06)	0.71 (0.01)
20161025-1	120.4	58.9	49	4.03	88.6 (90)	4.58 x 10^3	0.258	5.99 (0.05)	0.65 (0.01)
20161018-1	71.0	49.0	48	4.07	82.5 (80)	7.93 x 10^3	0.134	8.99 (0.01)	0.83 (0.02)
20161018-2	38.0	40.0	48	3.96	84.3 (80)	1.40 x 10^4	0.069	14.17 (0.10)	0.72 (0.02)
20151020-2	200.3	69.1	47	4.34	85.9 (90)	3.20 x 10^3	0.150	3.82 (0.05)	0.65 (0.03)
20151020-1	118.9	58.7	49	4.36	84.4 (80)	5.42 x 10^3	0.170	6.57 (0.13)	0.86 (0.04)
20151013-1*	70.1	48.7	47	4.36	80.5 (80)	9.22 x 10^3	0.067	10.26 (0.01)	0.71 (0.02)
20151027-1	37.5	39.9	49	4.33	84.9 (90)	1.70 x 10^4	0.033	17.47 (0.18)	0.81 (0.21)
20141209-4	163.0	68.6	56	7.13	86.6 (90)	1.06 x 10^4	0.093	8.39 (0.06)	0.71 (0.01)
20150715-3	51.0	49.4	63	6.95	80.3 (80)	3.21 x 10^4	0.044	22.72 (0.06)	–
20150715-4	27.0	39.9	63	6.91	86.5 (90)	5.99 x 10^4	0.025	33.25 (1.19)	–

a: Asterisks (*) indicate the results shown in Fig. 5b. Plus signs (+) indicate the results shown in Fig. 10a.

b: The numbers without parentheses indicate the impact angle measured by using the images observed by a high-speed camera or a shutter camera. The numbers in parentheses indicate the impact angle used in the text.

c: NLFM means the normalized largest fragment mass, which is the largest fragment mass normalized by the original target mass.

d: The numbers in parentheses indicate the error.

e: α is the power law index on the power law equation showing the mass frequency distributions of impact fragments. The numbers in parentheses indicate the error.

Table 2. Experimental conditions and results for glass targets

Run number [a]	Target		Impact velocity v_i, km s^{-1}	Impact angle θ^b, degree	Specific energy Q, J kg^{-1}	NLFM m_l/M_t[c]	Antipodal jet velocity V_{jet}[c], m s^{-1}	α^e
	Mass M_t, g	Diameter, mm						
Oblique impact: Target diameter = 80 mm, Impact velocity ~4.3 km s^{-1}								
20151119-1	671.3	79.6	4.19	76.6 (75)	8.88 x 10^2	0.631	159.90 (1.40)	0.89 (0.01)
20151028-1	662.8	79.3	4.34	59.1 (60)	9.64 x 10^2	0.679	197.04 (4.00)	0.92 (0.01)
20151008-2	626.8	77.9	4.38	46.8 (45)	1.04 x 10^3	0.833	163.52 (n.d.)	0.98 (0.01)
20151028-2	664.1	79.4	4.41	37.2 (40)	9.96 x 10^2	0.868	–	1.08 (0.01)
20151111-1	669.1	79.6	4.25	21.8 (20)	9.18 x 10^2	0.944	–	1.03 (0.02)
20151125-1	663.7	79.3	4.30	14.8 (15)	9.47 x 10^2	0.973	26.93 (n.d.)	0.99 (0.03)
Oblique impact: Target diameter = 50 mm, Impact velocity ~4.3 km s^{-1}								
20151029-2	163.1	50.1	4.32	72.9 (75)	3.88 x 10^3	0.046	210.64 (1.08)	1.03 (0.02)
20151008-1	163.7	50.2	4.39	57.3 (60)	3.99 x 10^3	0.028	153.76 (1.92)	1.00 (0.02)
20151022-1*	164.4	50.2	4.25	58.9 (60)	3.73 x 10^3	0.059	186.20 (3.58)	0.94 (0.02)
20151118-1*$^+$	162.7	50.0	3.96	41.9 (40)	3.26 x 10^3	0.203	150.38 (4.61)	0.88 (0.03)
20151022-2	160.0	49.8	4.39	32.1 (30)	4.08 x 10^3	0.479	164.90 (n.d.)	0.92 (0.02)
20151119-2*$^+$	154.8	49.3	4.37	28.4 (30)	4.19 x 10^3	0.562	156.64 (12.20)	0.95 (0.03)
20151202-1*$^+$	164.6	50.2	4.28	14.8 (15)	3.78 x 10^3	0.780	–	0.81 (0.01)
Oblique impact: Target diameter = 80 mm, Impact velocity ~5.9 km s^{-1}								
20170208-1	658.6	79.0	5.93	57.4 (60)	1.81 x 10^3	0.216	188.32 (8.07)	0.87 (0.01)
20170208-2	637.5	78.2	5.86	47.0 (45)	1.83 x 10^3	0.517	220.30 (2.63)	0.90 (0.01)
Oblique impact: Target diameter = 30 mm, Impact velocity ~4.9 km s^{-1}								
20160107-1	32.3	29.2	4.87	76.6 (75)	2.49 x 10^4	0.005	196.34 (3.79)	–

Table 2. Continued

Run number [a]	Target		Impact velocity v_i, km s^{-1}	Impact angle θ^b, degree	Specific energy Q, J kg^{-1}	NLFM $m_l/M_t{}^c$	Antipodal jet velocity $V_{jet}{}^c$, m s^{-1}	α^e
	Mass M_t, g	Diameter, mm						
Head-on collision								
20151209-1	668.7	79.5	2.17	89.5 (90)	2.39 x 10^2	0.943	56.20 (1.27)	–
20151203-2	164.9	50.3	2.13	81.6 (80)	9.32 x 10^2	0.586	111.66 (1.20)	–
20151007-1	586.5	76.0	4.17	83.7 (80)	1.00 x 10^3	0.733	–	0.93 (0.01)
20151001-1*+	164.7	50.3	4.14	80.5 (80)	3.53 x 10^3	0.040	177.12 (0.73)	0.93 (0.02)
20160107-2	669.0	79.6	4.93	80.8 (80)	1.24 x 10^3	0.391	264.03 (3.17)	1.00 (0.01)
20160106-1	278.8	59.5	4.94	88.6 (90)	2.97 x 10^3	0.029	211.27 (3.97)	1.13 (0.04)
20151202-2	655.6	79.0	6.00	84.4 (80)	1.86 x 10^3	0.210	223.65 (n.d.)	–
20170207-1	658.9	79.0	5.88	84.5 (90)	1.78 x 10^3	0.189	201.39 (3.24)	0.87 (0.01)
20151203-1	163.7	50.2	5.95	86.8 (90)	7.34 x 10^3	0.015	255.71 (n.d.)	–

a: Asterisks(*) indicate the results shown in Figs. 5c and 5d. Plus signs (+) indicate the results shown in Fig. 10b.

b: The numbers without parentheses indicate the impact angle measured by using the images observed by a high-speed camera or a shutter camera. The numbers in parentheses indicate the impact angle used in the text.

c: NLFM means the normalized largest fragment mass, which is the largest fragment mass normalized by the original target mass.

d: The numbers in parentheses indicate the error. “n.d.” means “not determined”.

e: α is the power law index on the power law equation showing the mass frequency distribution of impact fragments. The numbers in parentheses indicate the error.

Table 3. Parameters p_1 and q_1 of Eq. (2) and impact strength Q^* at head-on collisions (θ =90° and 80°)

Target	p_1	q_1	Q^* [J kg^{-1}]
Porous gypsum: this study	2.32 (0.31)	0.84 (0.08)	1.33 (0.47) × 10^3
Glass: this study	5.82 (0.70)	2.02 (0.21)	1.07 (0.19) × 10^3
Porous gypsum: *Okamoto and Arakawa* [2009]	2.66 (0.55)	0.87 (0.14)	2.42 (0.84) × 10^3
Basalt: *Fujiwara and Tsukamoto* [1980]	4.40 (0.68)	1.53 (0.18)	1.17 (0.78) × 10^3

Numbers in parentheses are the standard deviation.

The parameters p_1 and q_1 in this study were obtained at the $m_\mathrm{l}/M_\mathrm{t}$ <0.75.

Table 4. Parameters p_2 and q_2 of Eq. (4) and effective impact strength $Q_{\mathrm{eff}}{}^*$

Target	Range of $m_{\mathrm{l}}/M_{\mathrm{t}}$ (NLFM)	p_2	q_2	$Q_{\mathrm{eff}}{}^*$ [J kg^{-1}]
Porous gypsum: this study	< 0.75	2.02 (0.22)	0.76 (0.06)	1.14 (0.47) × 10^3
Glass: this study	> 0.75	0.12 (0.10)	0.08 (0.04)	9.07 (2.30) × 10^2
	< 0.75	4.66 (0.39)	1.68 (0.12)	
Basalt: *Fujiwara and Tsukamoto* [1980]	–	4.17 (0.40)	1.50 (0.11)	9.42 (4.08) × 10^2

Numbers in parentheses are the standard deviation.

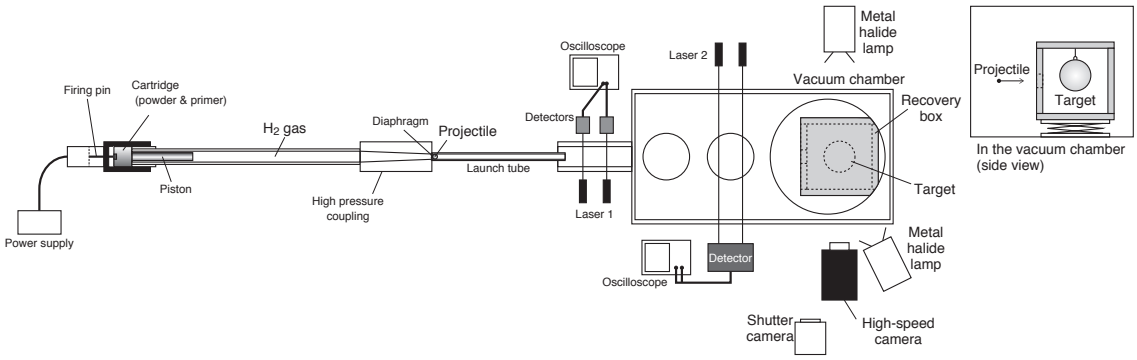

Fig. 1

Yasui et al.

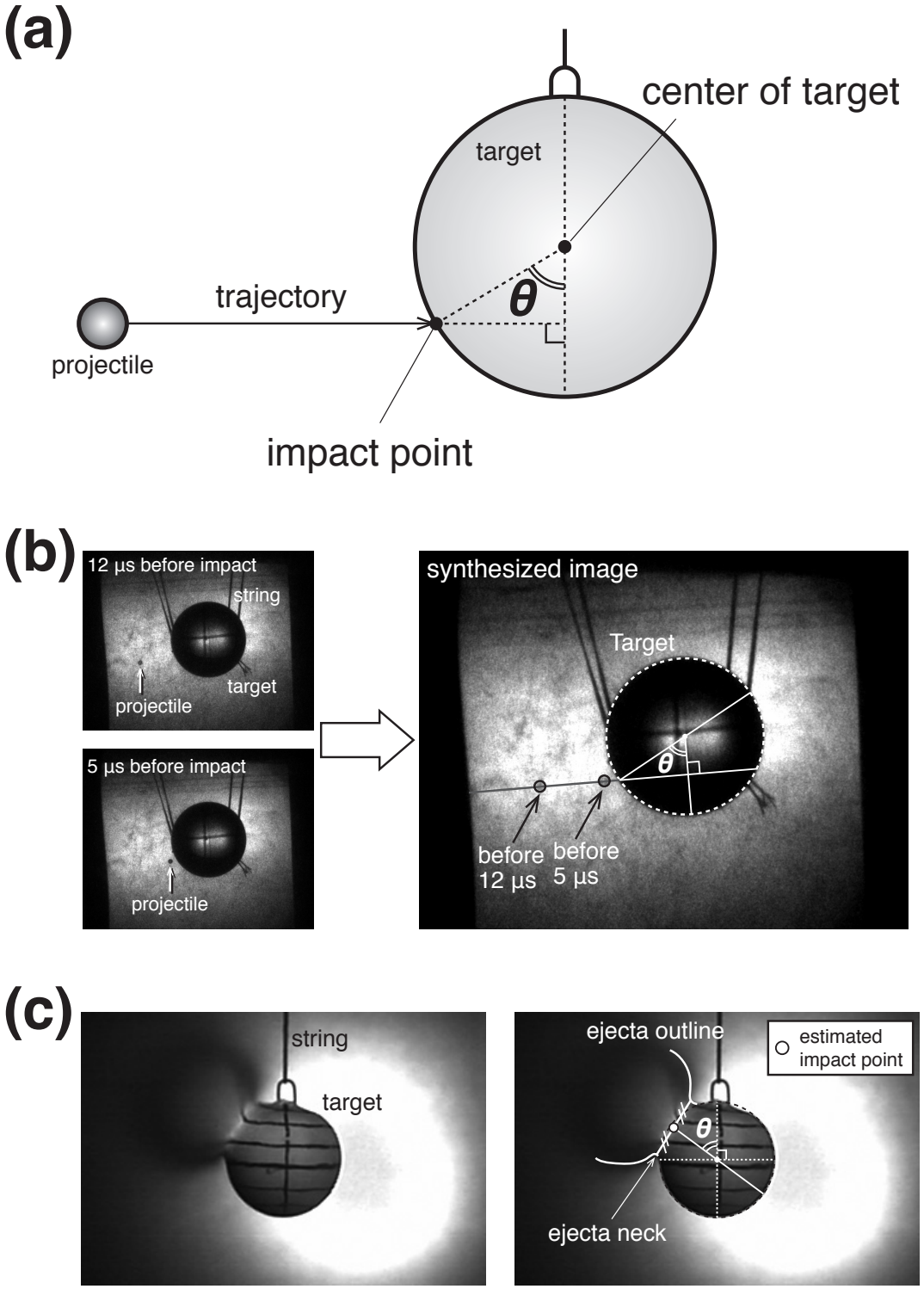

Fig. 2

Yasui et al.

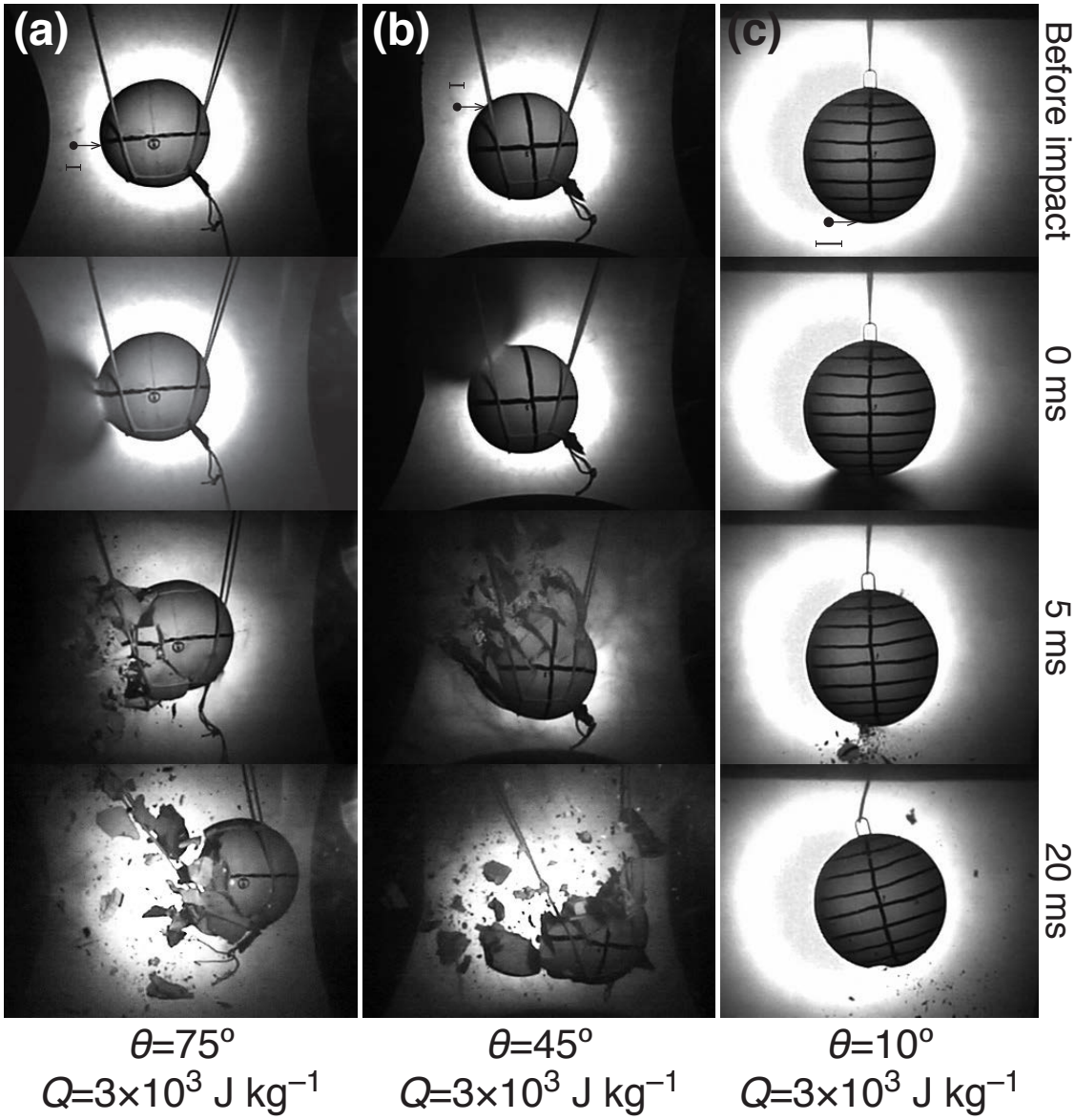

Fig. 3a–c

Yasui et al.

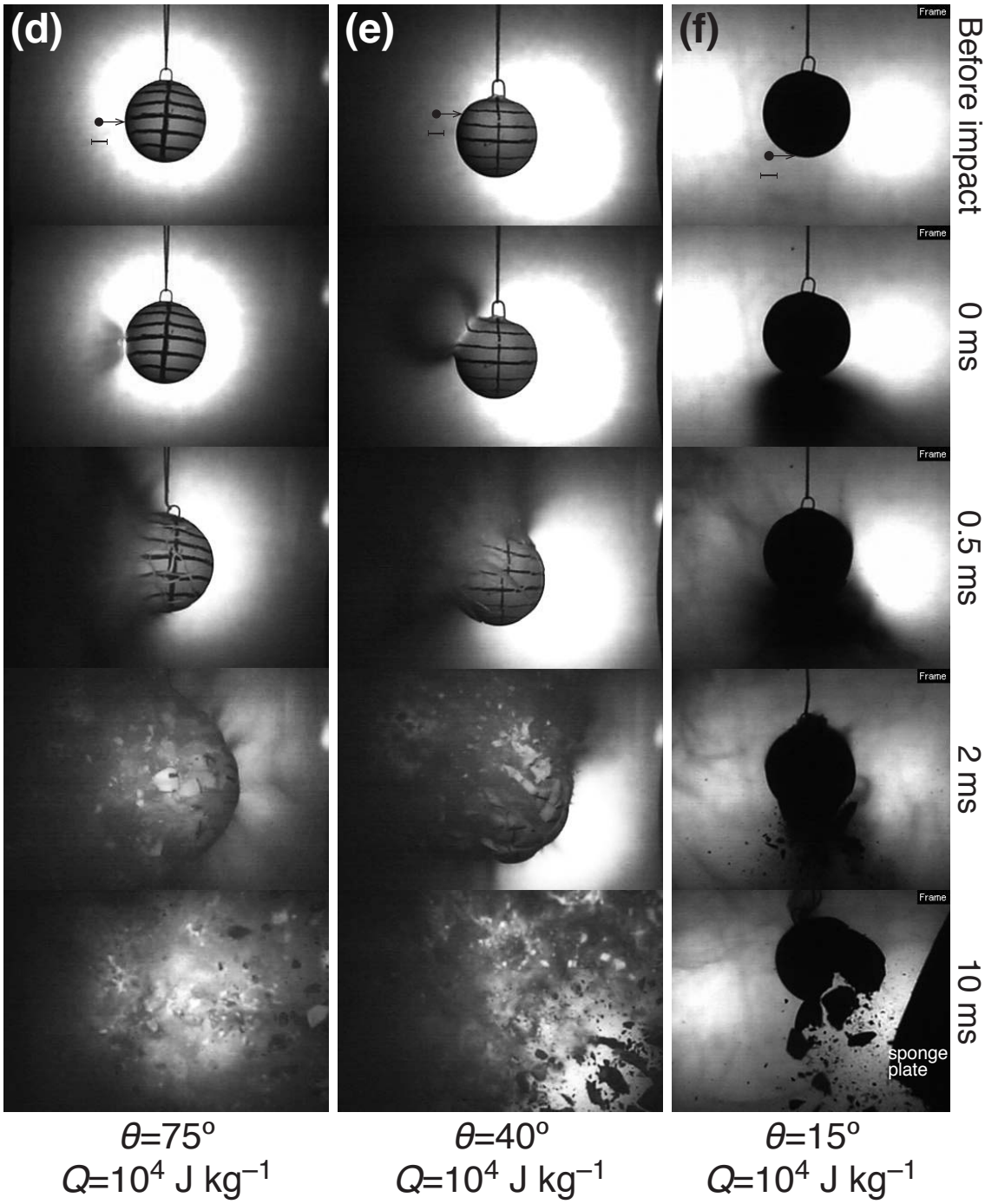

Fig. 3d–f

Yasui et al.

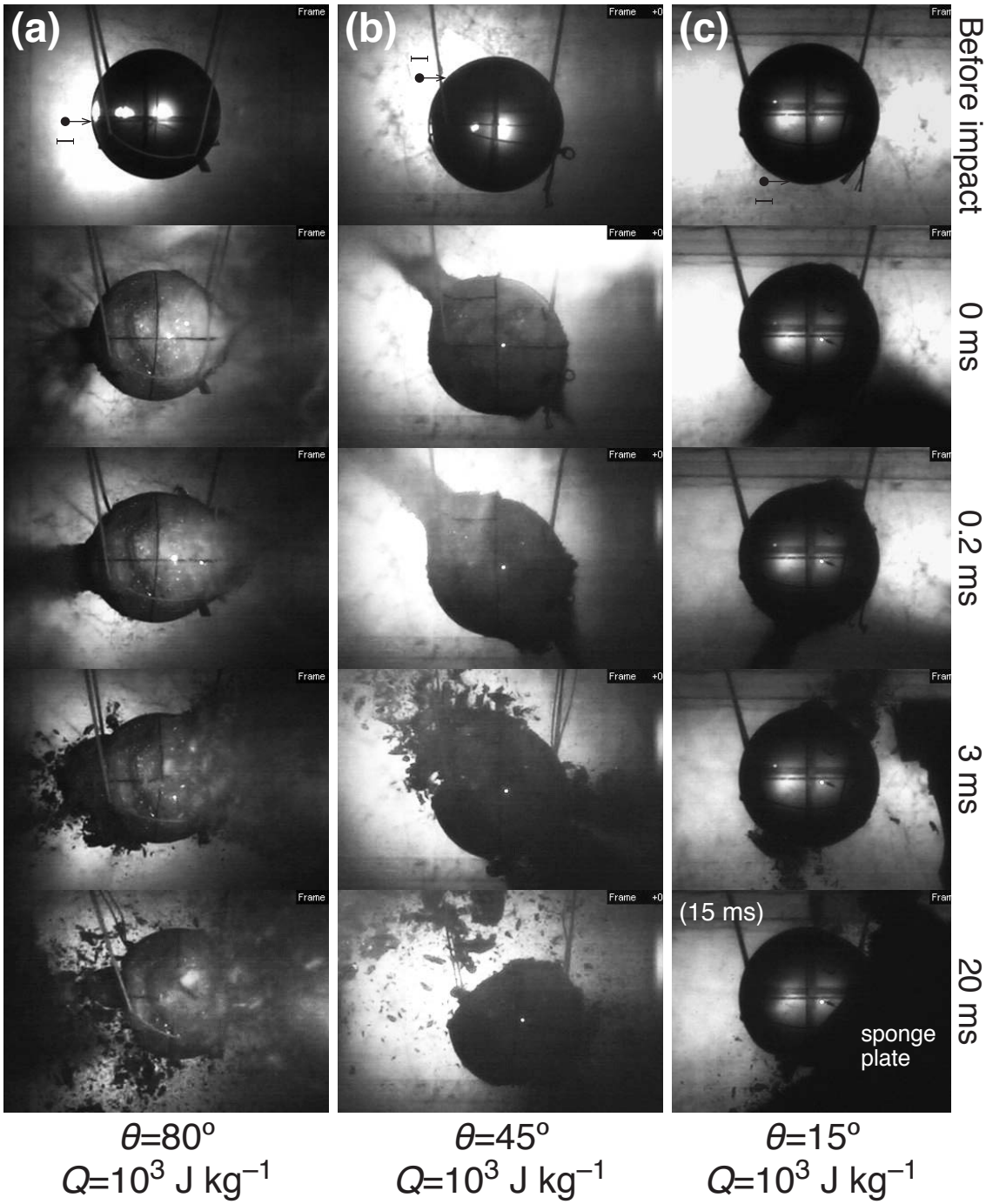

Fig. 4a–c

Yasui et al.

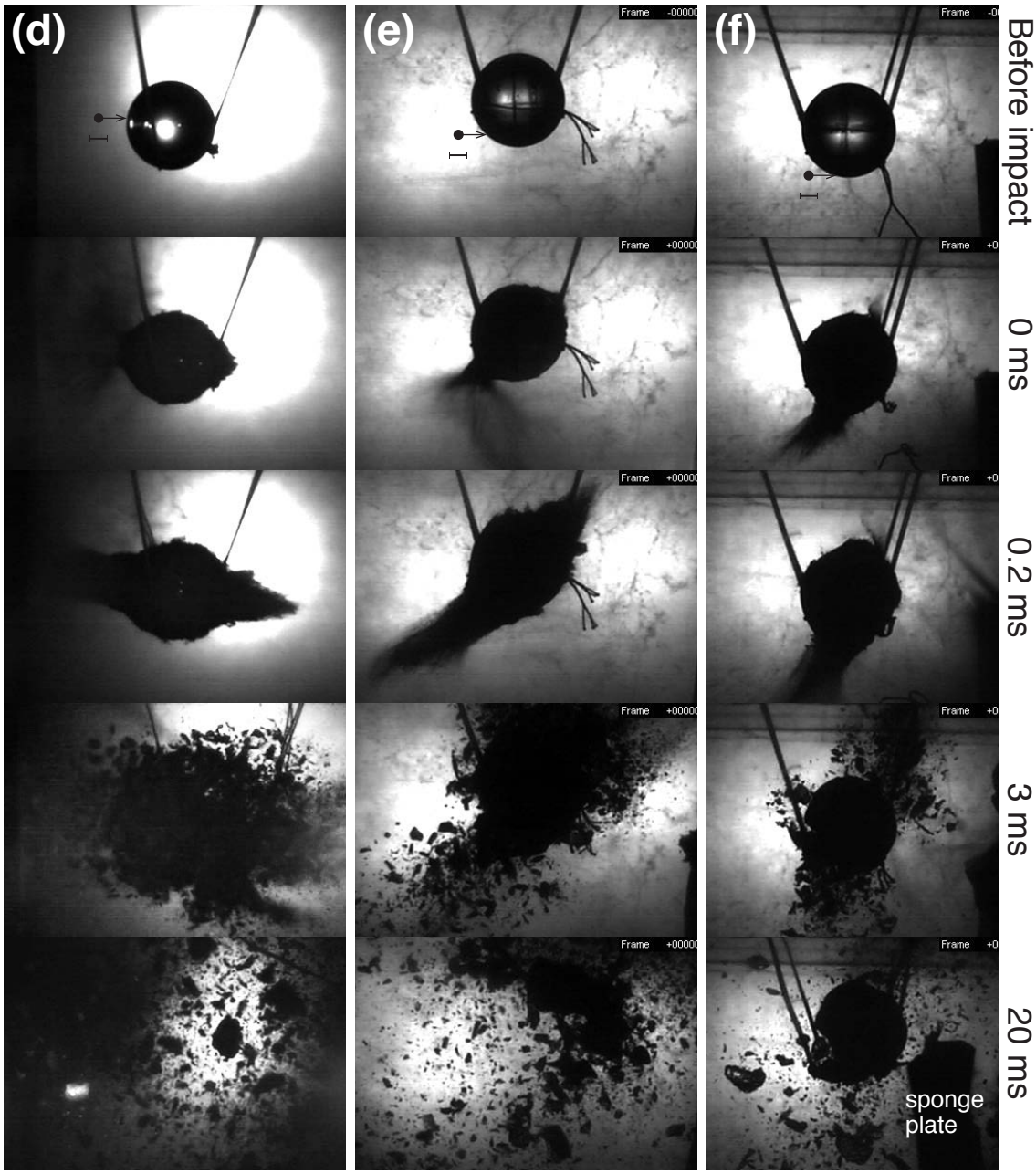

Fig. 4d–f

Yasui et al.

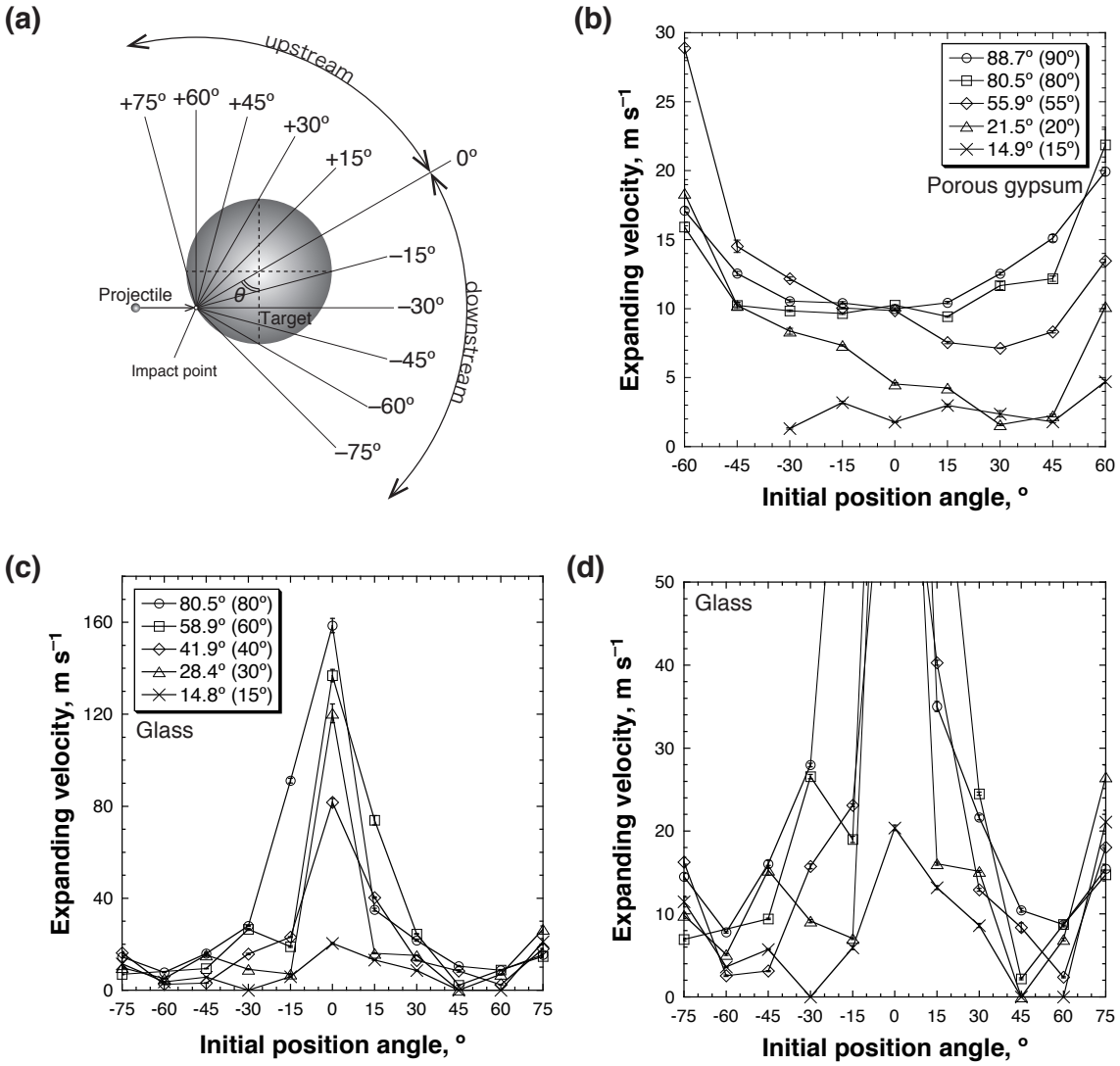

Fig. 5

Yasui et al.

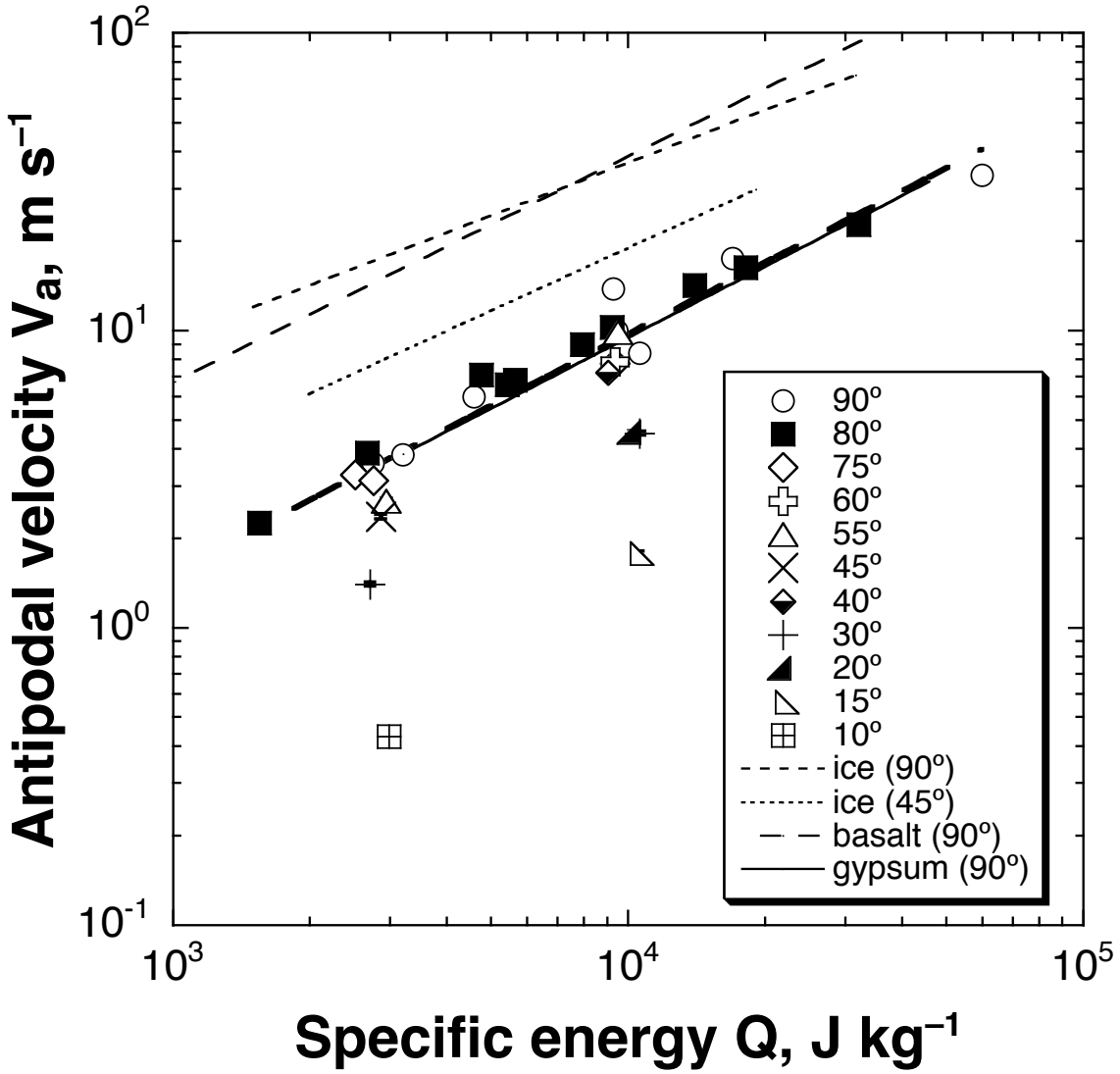

Fig. 6

Yasui et al.

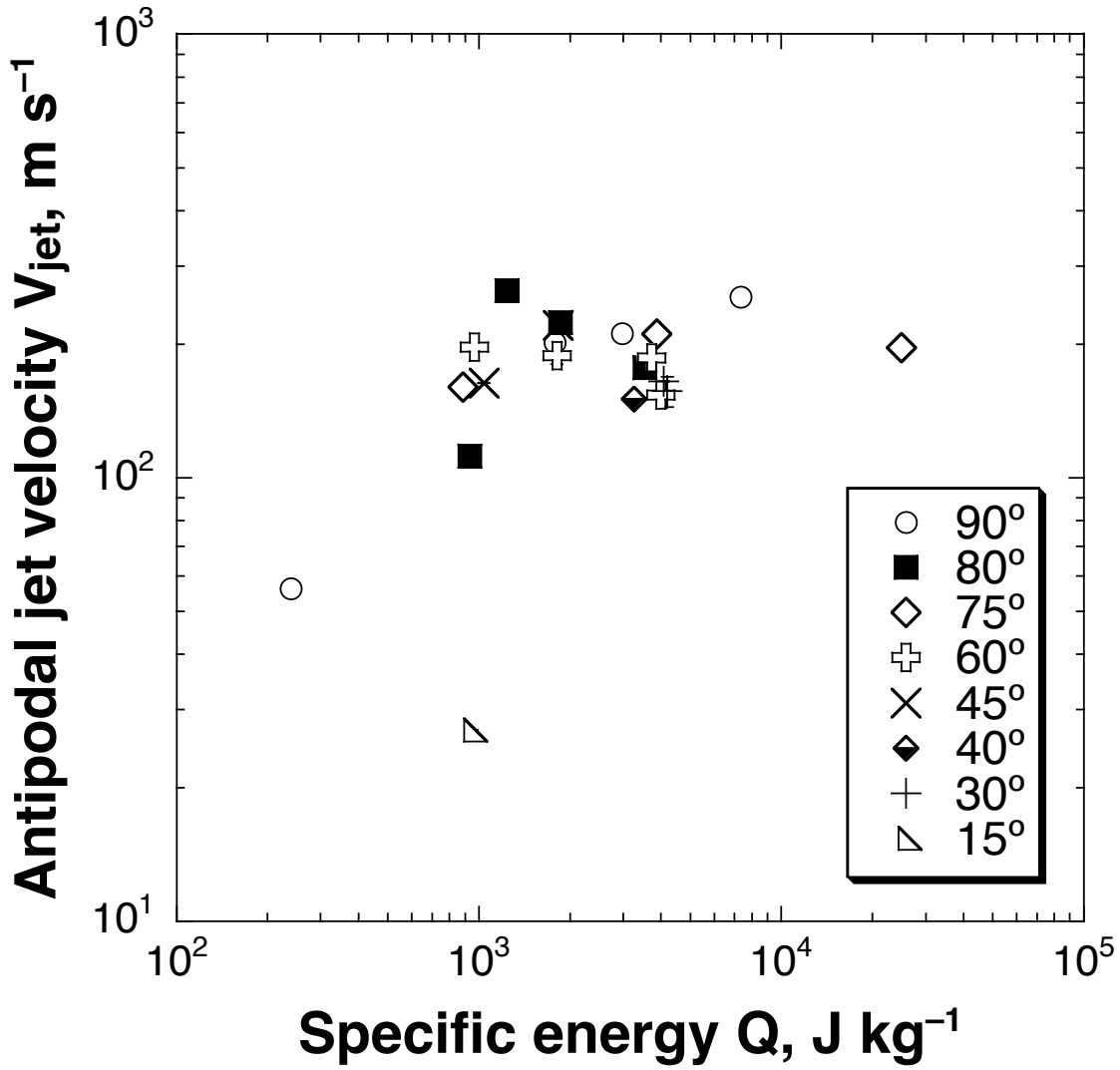

Fig. 7

Yasui et al.

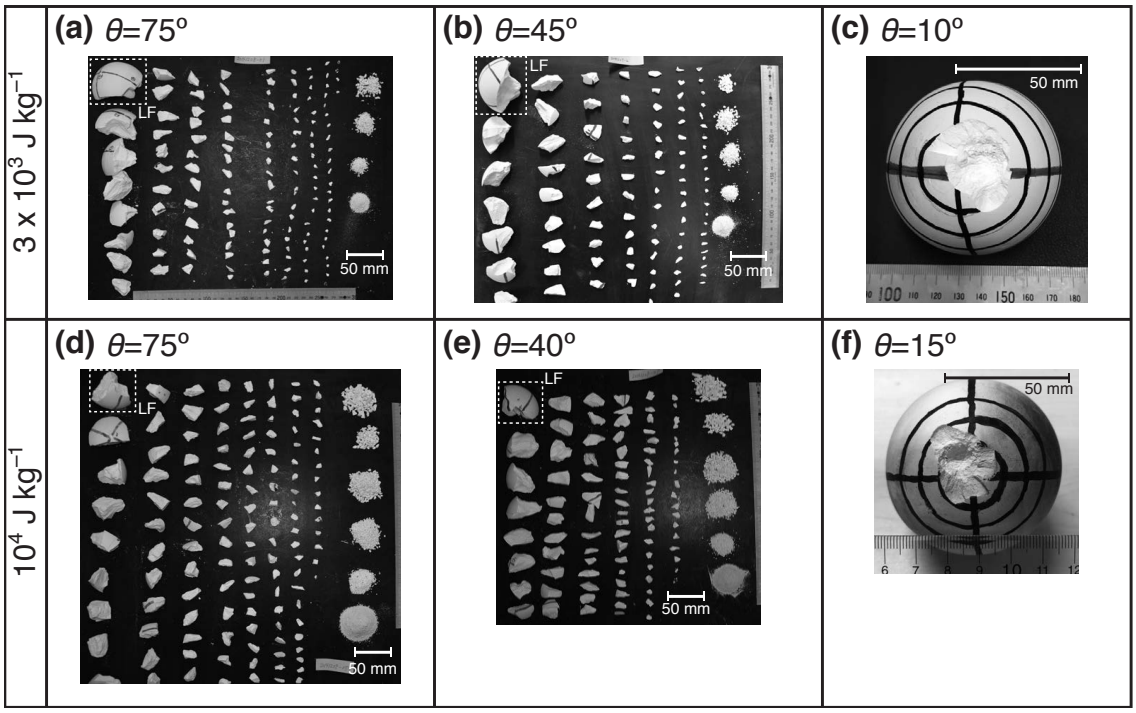

Fig. 8

Yasui et al.

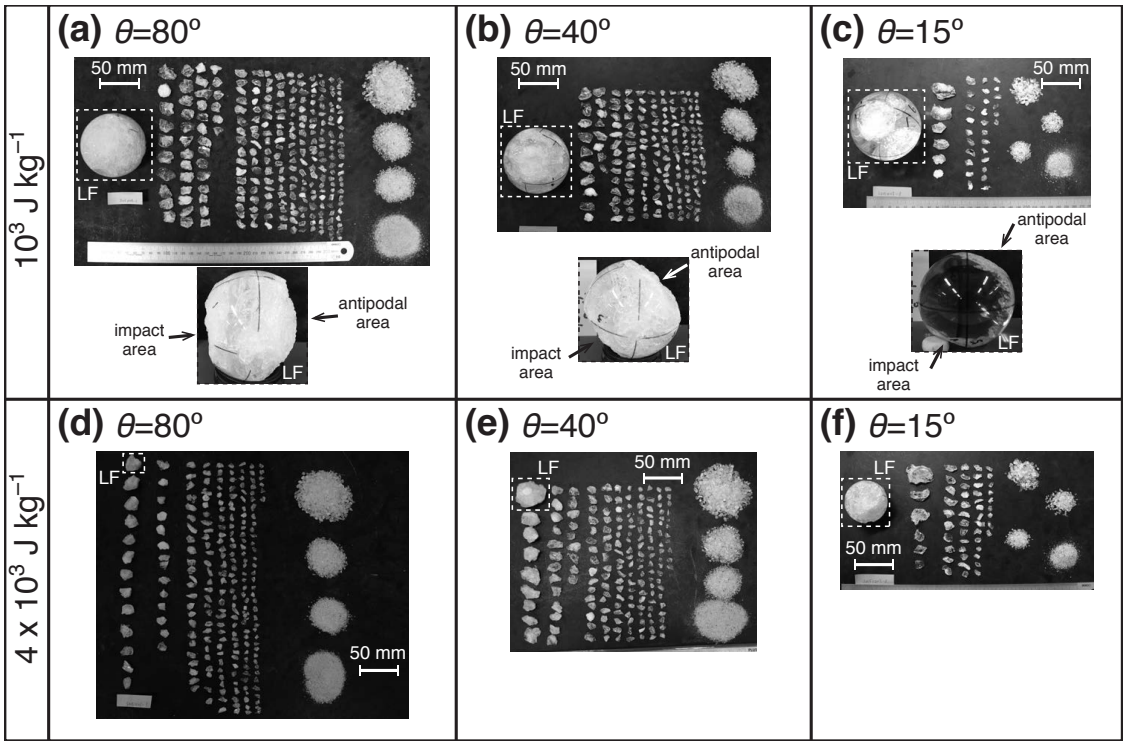

Fig. 9

Yasui et al.

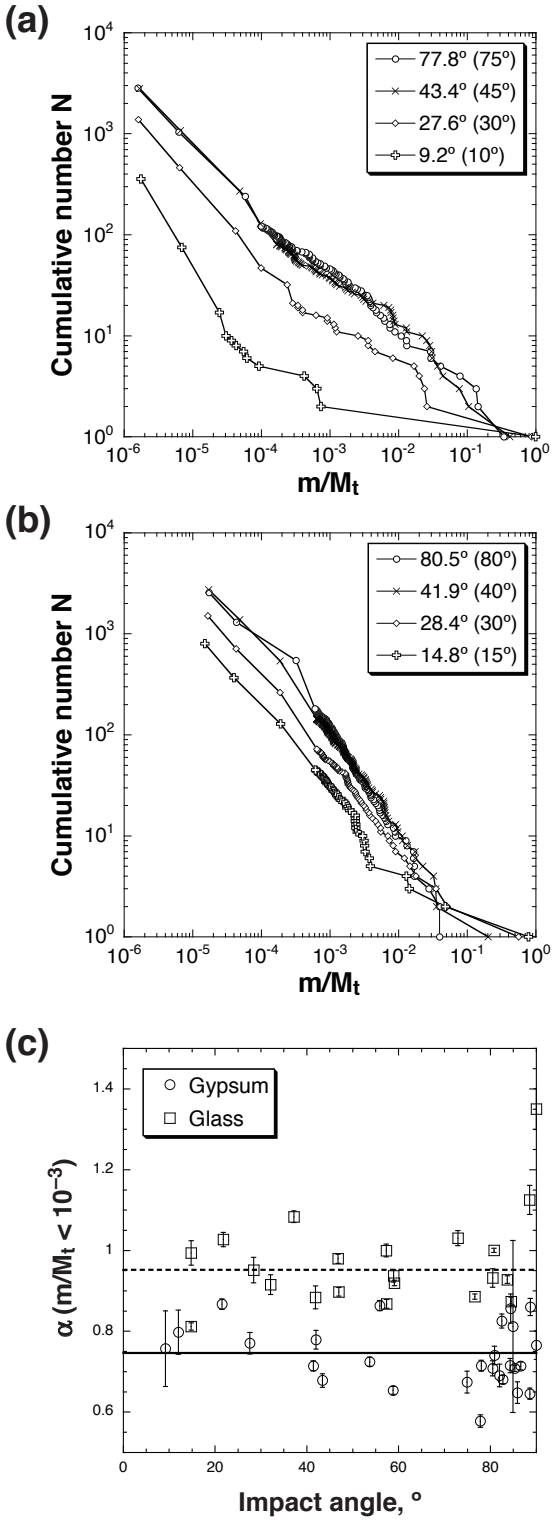

Fig. 10

Yasui et al.

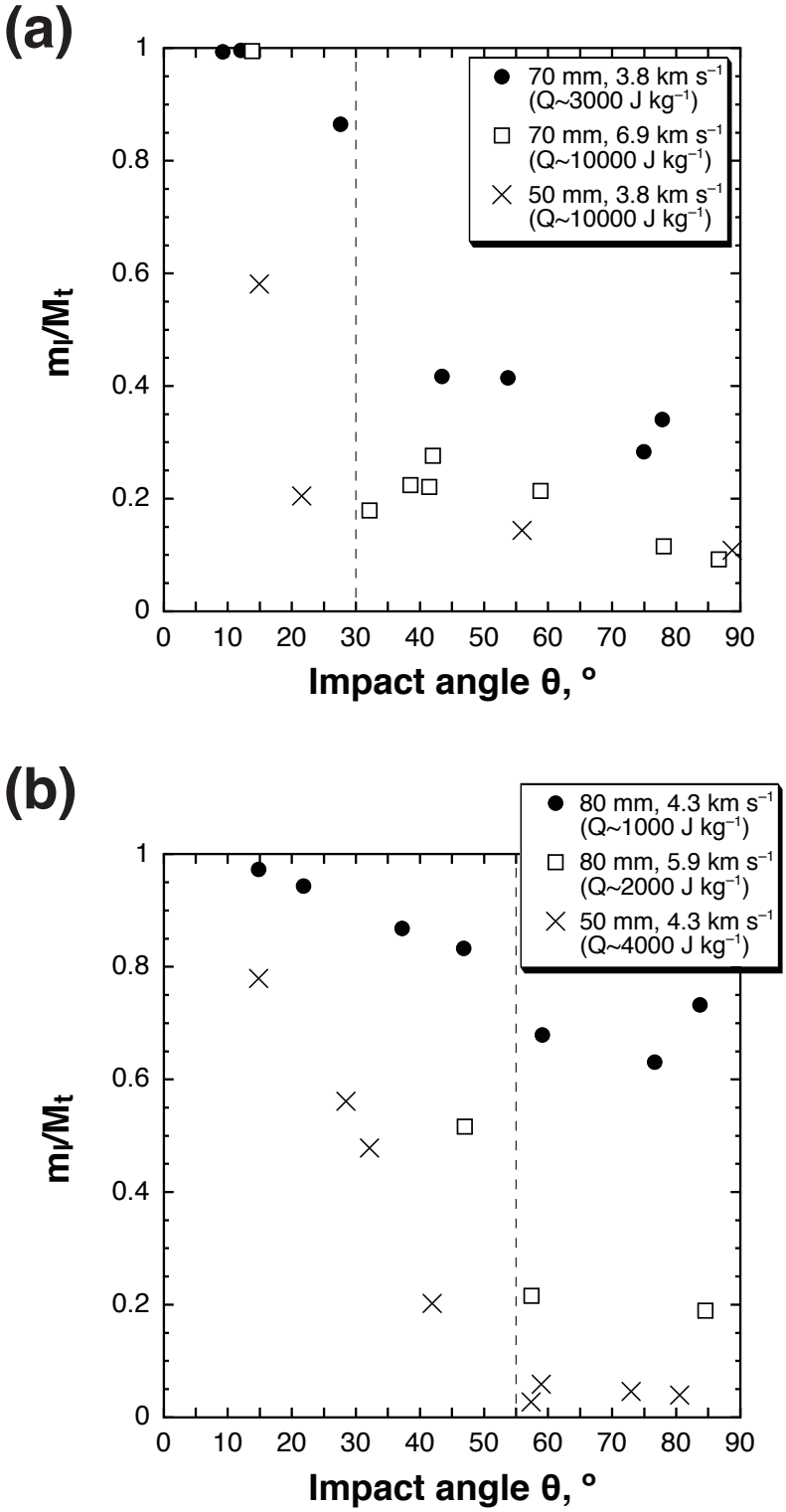

Fig. 11

Yasui et al.

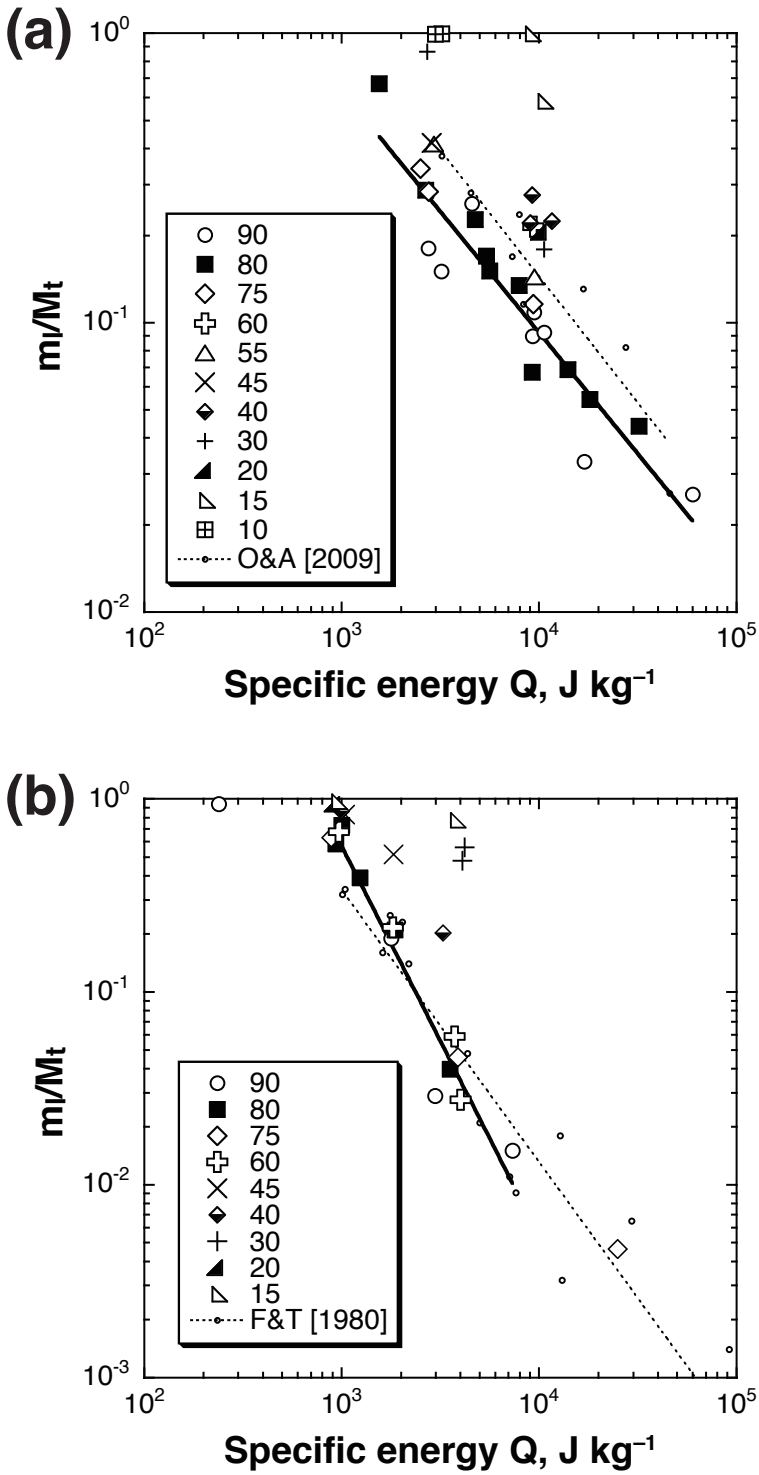

Fig. 12

Yasui et al.

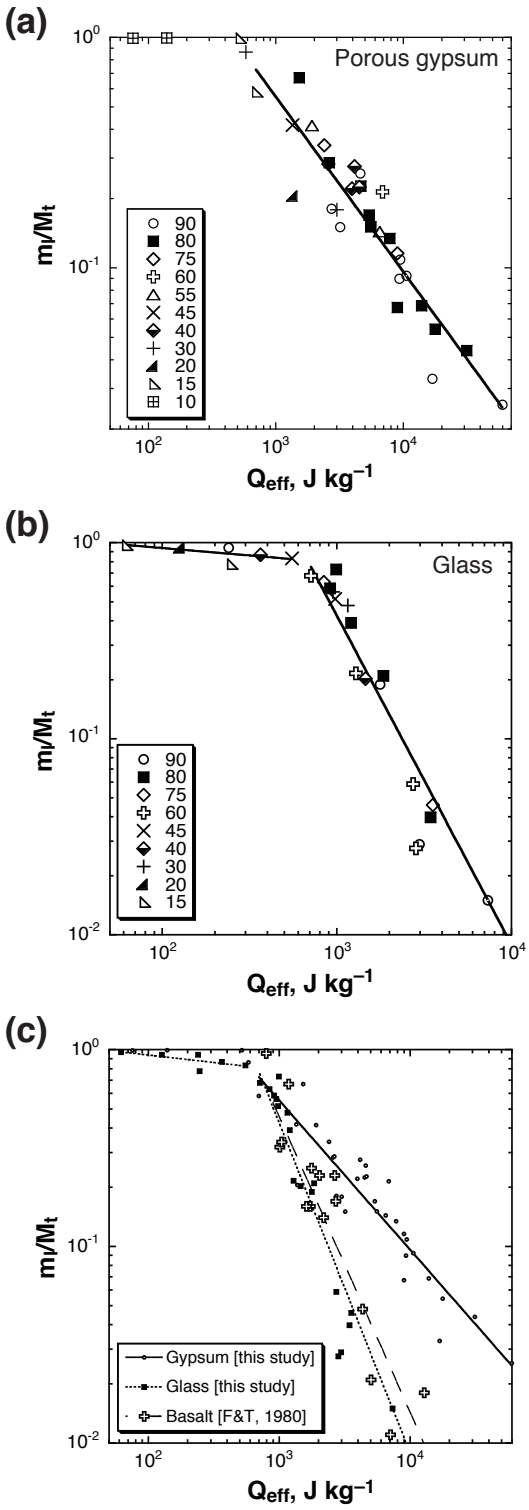

Fig. 13

Yasui et al.

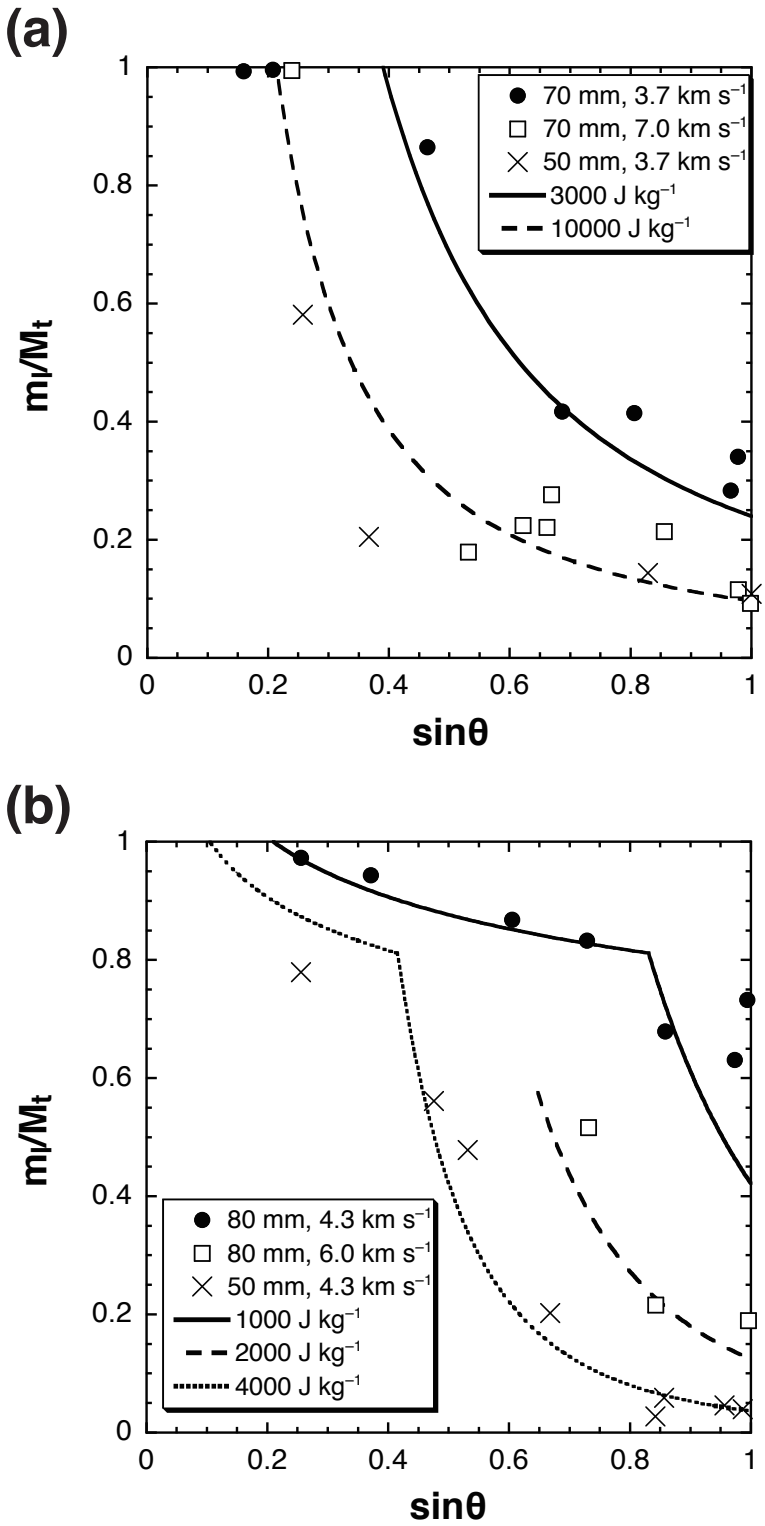

Fig. 14

Yasui et al.

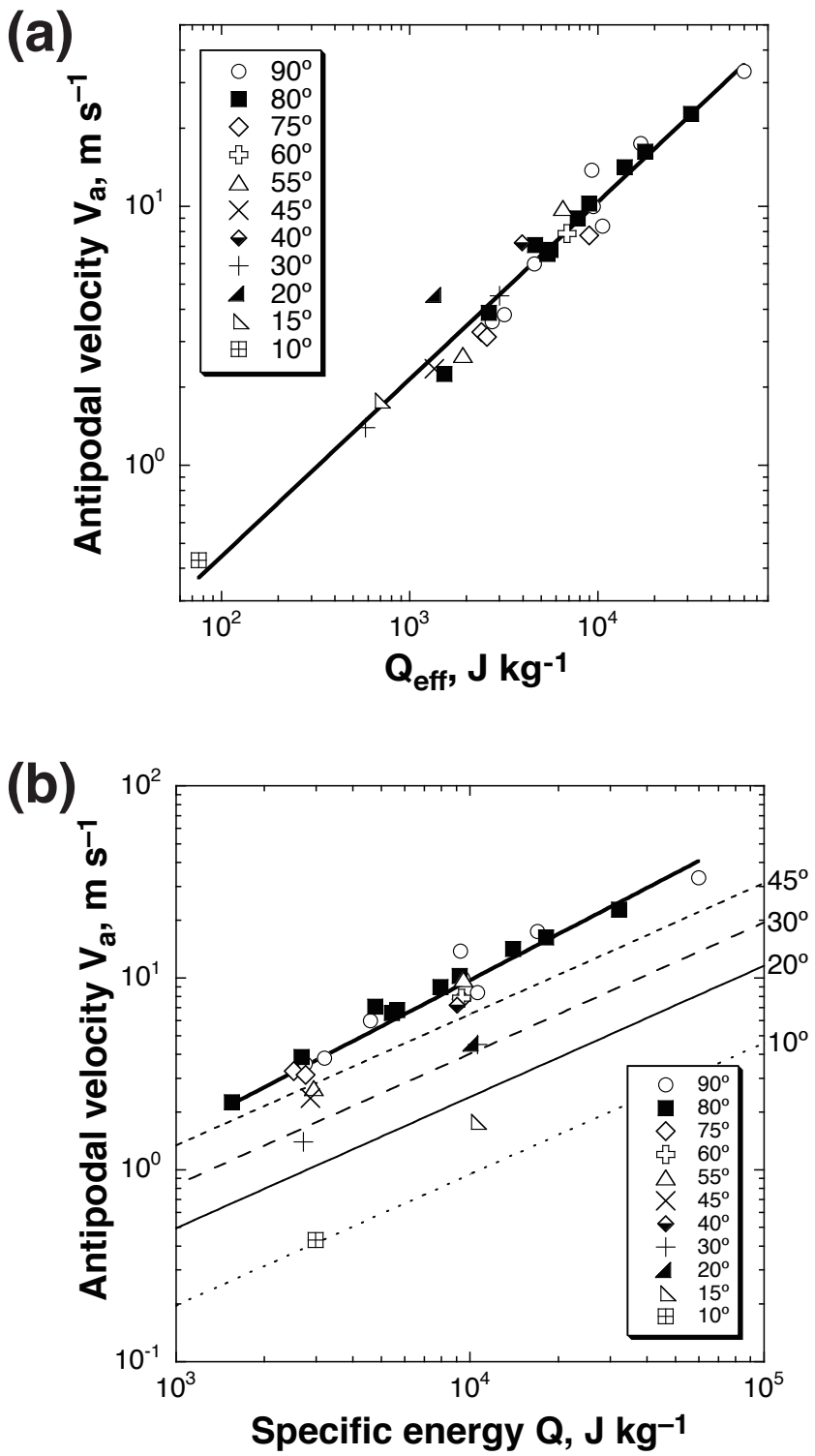

Fig. 15

Yasui et al.

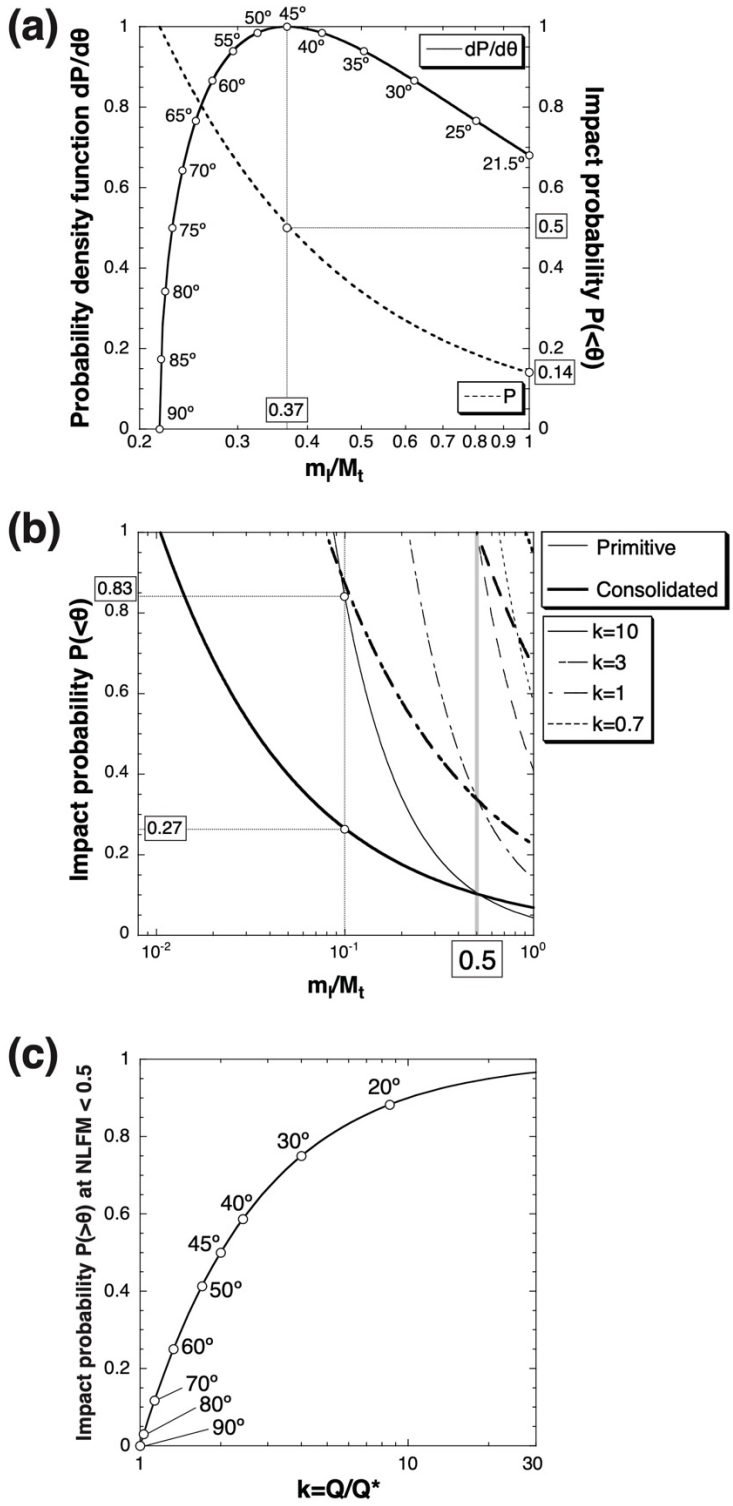

Fig. 16

Yasui et al.